Large eddy simulation of combustion instability in a subcritical hydrogen peroxide/kerosene liquid rocket engine: Intermittency route to period-2 thermoacoustic instability ⊘

Liu Yuanzhe (刘远哲) ⓘ ; Liu Peijin (刘佩进) ⓘ ; Wang Zhuopu (王琢璞) ✉ ⓘ ; Ao Wen (敖文);
Guan Yu (关昱) ⓘ

Check for updates

View Online   Export Citation

Physics of Fluids

Special Topics Open for Submissions

Learn More

AIP Publishing

Physics of Fluids

AIP Publishing

Large eddy simulation of combustion instability in a subcritical hydrogen peroxide/kerosene liquid rocket engine: Intermittency route to period-2 thermoacoustic instability

Yuanzhe Liu (刘远哲),[1] [iD] Peijin Liu (刘佩进),[1] [iD] Zhuopu Wang (王琢璞),[1,a)] [iD] Wen Ao (敖文),[1] and Yu Guan (关昱)[2] [iD]

AFFILIATIONS

[1]Science and Technology on Combustion, Internal Flow and Thermal-Structure Laboratory, Northwestern Polytechnical University, Xi'an 710072, China
[2]Department of Aeronautical and Aviation Engineering, The Hong Kong Polytechnic University, Kowloon, Hong Kong

[a)]Author to whom correspondence should be addressed: zpwang@nwpu.edu.cn

ABSTRACT

This paper presents the first numerical evidence of an intermittency route to period-2 thermoacoustic instability in a subcritical single-element liquid rocket engine burning hydrogen peroxide/kerosene as we decrease the equivalence ratio (ϕ) from fuel-rich to fuel-lean. To achieve this, three-dimensional compressible large eddy simulation algorithms combined with the Euler–Lagrangian framework are used. A one-equation eddy sub-grid turbulence model with a partially stirred reactor sub-grid combustion model is employed to simulate the spray turbulent combustion process in a high-pressure liquid-fueled combustor based on open-source platform OpenFOAM. This paper focuses on examining the transition process of the dynamical states in the thermoacoustic system and the synchronization between multiple subsystems. The results indicate that, as the equivalence ratio reduces continuously ($1.5 \leq \phi \leq 0.5$), the system dynamics shift from period-1 oscillations ($\phi = 1.5$) to period-2 oscillations ($\phi = 0.5$) via intermittency ($1.3 \leq \phi \leq 0.9$). Under the equivalence ratio of 0.7 ($\phi = 0.7$), a transient mode switching between period-1 and period-2 was also observed. The synchronization processes between the pressure and combustion subsystems in terms of phase-locking and frequency-locking are responsible for the emergence of complex dynamical states. The cycle snapshots analysis also provides more details on the synchronization processes between the pressure and the multiple subsystems, such as vortex dynamics, mixture fraction, and combustion heat release. In summary, this paper sheds light on the complex non-linear thermoacoustic oscillations and the underlying physical mechanisms related to the two-phase flow of spray combustion in liquid rocket engines using three-dimensional large eddy simulations, paving the way for developing passive or active control methods.

I. INTRODUCTION

The emergence of combustion instabilities (CIs) has been a major challenge for the development of industrial combustion equipment, such as gas turbines, aero-engines, solid rocket motors, and liquid rocket engines.[1–5] During CIs, large amplitude periodic acoustic oscillations can occur in the combustion chamber, which in turn cause catastrophic damage to the combustion equipment, such as increased heat transfer, thrust oscillations, and even structural damage. CIs are the more serious problem in liquid rocket engines because the high energy density in the combustion chamber makes it easier to establish a positive feedback loop between unsteady combustion, hydrodynamic instability, and acoustics.[6,7] As a result, investigating CIs in liquid

rocket engines and the corresponding suppression measures has been a key issue in the rocket propulsion community over the years.[8,9]

Although a great deal of research on the CIs of liquid rocket engines has been carried out since the 1950s,[10] a thorough and comprehensive understanding of the phenomenon of CIs is still lacking. CIs in liquid rocket engines are a highly non-linear physical process involving the coupling of multiple sub-processes, such as injection, atomization, evaporation, hydrodynamics, combustion, and acoustics.[9,11,12] The mechanisms driving combustion instability are complex depending on the particular engine configuration and its operating conditions. The longitudinal combustion instability of a liquid rocket engine with a single-element coaxial injector is of interest in this paper,

as it has a simple structure and can also be the most faithful representation of the physical environment of a full-size engine.[13] In coaxial liquid rocket engines, vortices are formed at the shear layer due to the interaction of high and low-speed flows.[14] The flow separation phenomenon between the high-speed flow containing unburned reactants and the low-speed flow consisting of many hot products leads to the formation of a recirculation zone downstream of the dump plane and, thus, acts as a stabilization mechanism for the flame. Vortex structures can have a significant effect on the geometry of the flame surface, while vortex shedding can also generate acoustic waves.[15] The shear layer is excited by the acoustic waves, which in turn leads to oscillations in the heat release rate. The oscillation of the heat release rate has a further effect on the acoustic field, either as a damping or a driving effect.[16] It is now widely accepted in both industry and academia that when an appropriate phase relationship exists between the heat release rate oscillations and the pressure oscillations, the oscillations will be amplified and the opposite will be suppressed, as proposed by Lord Rayleigh.[17] In recent years, longitudinal combustion instability has become an increasing concern in the development of coaxial liquid rocket engines, due to the coupling effect between the combustion chamber and the coaxial injector. These oscillations are not easily suppressed by traditional transverse baffles. The research work in this paper is related to longitudinal combustion instability driven by vortex shedding and discusses the self-excited instabilities due to changes in control parameters.

The transition of the system dynamics from a combustion noise state to a thermoacoustic instability state due to changes in the control parameters is made via Hopf bifurcation.[18] The traditional view was generally that the dynamical states of the system were either a fixed point (combustion noise) or a limit cycle state with simple period-1 oscillation (thermoacoustic instability). When the system is in a state of period-1 (P1) limit cycle, the oscillation is restricted to a constant amplitude and a single frequency. Based on this understanding, many predictive tools have been developed to assess the linear or nonlinear stability of thermoacoustic systems.[19–21] The best known of these are the methods of linear acoustic control equations combined with linear flame models to predict unstable frequencies and corresponding acoustic modes at the onset of oscillation.[22] However, it is only recently that the dynamical state of thermoacoustic systems has been reported to be far more complex than the limit cycle.[23] As the amplitude of the oscillations increases, the mechanisms of non-linearity begin to become active and eventually dominate the dynamics of the system due to its nonlinear nature, proceeding to the emergence of complex nonlinear states that are not yet fully understood. It is necessary and urgent for researchers to understand complex dynamical states beyond the fixed point and simple period-1 oscillation states, as it directly influences and even over turns the current stage of predictive tools and passive or active control measures of combustion instability in liquid rocket engines.

It is only in recent years that increasing research has embraced the use of nonlinear time series analysis methods derived from the complex system approach, leading to the discovery of dynamical states far more complex than period-1 oscillations.[24] Recent developments include the application of a complex system approach to the characterization of nonlinear thermoacoustic oscillations and the identification of dynamical states by research groups represented by Sujith[1,25–31] and Gotoda.[32–35] Even in a simple laminar thermoacoustic system with

duct-premixed flame, the dynamical state of the system undergoes multiple bifurcations as the control parameters (the position of the flame within the duct) are continuously varied, leading to the emergence of period-1 oscillations, quasi-periodicity, intermittency, frequency-locking, chaos, and period-n.[26] Based on such a simple experimental thermoacoustic system, researchers have established three routes to chaos: the quasi-periodic route,[29] the frequency-locked quasi-periodic route,[36] and the intermittency route to chaotic thermoacoustic instability.[37] However, for more industrialized rocket engines, high Reynolds numbers, molecular scale mixing, and high energy densities introduce greater complexity for thermoacoustic systems. Thermoacoustic systems in rocket engines also exhibit complex pressure oscillations that cannot be described by the classical Hopf bifurcation. Using nonlinear time series analysis, Guan et al.[38] reported the transition of the dynamical state between period-2 and period-3 during the onset of thermoacoustic instability in a solid rocket motor. Kasthuri et al.[39] also reported that the transition from stable operating conditions to thermoacoustic instability was made via intermittency in liquid rocket experiments. The two studies mentioned above were limited to the analysis of time series of pressure measured by experiment lacking simultaneous examination of the combustion flow fields. Shima et al.[40] investigated the formation mechanism of high-frequency combustion oscillations in the combustion chamber of a model liquid rocket engine from the perspective of symbolic dynamics. The directional feedback between the pressure and combustion oscillations was identified using the directionality index of the symbolic transfer entropy. Kasthuri et al.[13] investigated spatiotemporal flame dynamics during the onset of transverse instability in a liquid rocket engine using a complex network approach. Although the simultaneous examination of combustion flow fields during period-1 thermoacoustic instability in liquid rocket engines has been studied, to our knowledge, there is still a lack of research on combustion flow fields in complex dynamical states. The simultaneous examination of combustion flow fields for complex dynamical states, such as period-n, intermittency, chaos and quasi-periodicity, could pave the way for the suppression of thermoacoustic instabilities in complex dynamical states.

In summary, recently, there has been increasing evidence indicating the presence of more intricate nonlinear dynamical states, such as intermittency, period-n, quasi-periodicity, and chaos, beyond simple period-1 oscillations (i.e., a limit cycle) in various thermoacoustic systems. During progressive changes in the control parameters, the thermoacoustic system undergoes various bifurcations leading to different nonlinear dynamical states. However, for a particular engine configuration and its operating conditions, the transition of the system dynamics due to non-linear mechanisms remains to be addressed. It is urgent to understand the transition process of non-linear dynamical states in liquid rocket engines. This is because non-periodic thermoacoustic oscillations contain multiple frequencies and, hence, different time scales, leading to the fact that neither current suppression measures nor reduced-order modeling tools have yet been adapted to such nonlinear aperiodic-1 oscillations. It is, therefore, necessary to investigate the dynamics of multiple bifurcation processes in a thermoacoustic system under typical operational environments of liquid rocket engines.

The first aim of this paper is to explore whether complex dynamical states exist in coaxial liquid rocket engines beyond simple period-1 oscillations. The global equivalence ratio is an important parameter in the liquid rocket community, as it is a measure of the ratio of the

actual fuel-oxidizer mixture ratio to the stoichiometric mixture ratio in the combustion chamber. If the mixture is too fuel-lean (low equivalence ratio), the combustion process may become unstable and lead to combustion oscillations, which can damage the engine or even cause it to fail. If the mixture is too fuel-rich (high equivalence ratio), the combustion process can become unstable as well, leading to flameouts or combustion instabilities. Therefore, this paper is focused on the effect of the equivalence ratio on the transition process of the dynamical state in the thermoacoustic system. The equivalence ratio is used as a control parameter and is continuously varied to encompass from fuel-rich to fuel-lean. Here, we present the first numerical evidence of an intermittency route to period-2 thermoacoustic instability in a subcritical single-element liquid rocket engine burning hydrogen peroxide/kerosene. The second aim of this paper is the simultaneous examination of the combustion flow fields of thermoacoustic systems in different dynamical states. Toward this purpose, three-dimensional large eddy simulation (LES) combined with the Eulerian–Lagrangian framework are used as a research strategy as this provides high-fidelity simulations of combustion instabilities and detailed information on the combustion flow field in liquid rocket engines. We perform the post-process analysis between several subsystems of the combustion flow field in different dynamical states from the point of view of vortex dynamics, synchronization processes between heat release rates and pressures, and cycle analysis of the combustion flow field. A comprehensive numerical investigation is performed to provide an in-depth understanding of the multi-bifurcation processes and the underlying physical mechanisms in liquid rocket engines with asymptotic changes in equivalence ratios, paving the way for active control measures of elaborate aperiodic thermoacoustic oscillations.

II. NUMERICAL FRAMEWORK
A. Governing equations and sub-grid models

The turbulent spray combustion processes were modeled using the Eulerian–Lagrangian approach within the framework of a complete three-dimensional large eddy simulation. The gas phase was mathematically described using spatially filtered compressible three-dimensional Navier–Stokes equations, in which the sub-grid turbulence effect was treated using a one-equation eddy model.[41,42] The liquid phase was considered as a discrete phase, while the droplet trajectory was tracked based on a Lagrangian framework. The flow variable $f(x,t)$ can be decomposed as $f(x,t) = \overline{f}(x,t) + \tilde{f}(x,t)$, where $\overline{f}(x,t)$ is the low-pass filter variable and $\tilde{f}(x,t)$ is the sub-grid variable. The mathematical expression for the filtered compressible Navier–Stokes equations is as follows:

$$\frac{\partial \overline{\rho}}{\partial t} + \frac{\partial \overline{\rho} \tilde{u}_j}{\partial x_j} = \overline{S}_{mass}, \quad (1)$$

$$\frac{\partial \overline{\rho} \tilde{u}_j}{\partial t} + \frac{\partial \left(\overline{\rho} \tilde{u}_i \tilde{u}_j \right)}{\partial x_i} + \frac{\partial \overline{p}}{\partial x_j} = \frac{\partial \left(\overline{\tau}_{ij} - \overline{\rho} \left(\widetilde{u_i u_j} - \tilde{u}_i \tilde{u}_j \right) \right)}{\partial x_i} + \overline{S}_{momentum}, \quad (2)$$

$$\frac{\partial \overline{\rho} \tilde{h}_s}{\partial t} + \frac{\partial \left(\overline{\rho} \tilde{u}_i \tilde{h}_s \right)}{\partial x_i} = \frac{\overline{Dp}}{Dt} + \frac{\partial}{\partial x_i} \left[\lambda \frac{\partial T}{\partial x_i} - \overline{\rho} \left(\widetilde{u_i h_s} - \tilde{u}_i \tilde{h}_s \right) \right]$$
$$+ \overline{\tau_{ij} \frac{\partial u_i}{\partial x_j}} - \frac{\partial}{\partial x_i} \left(\overline{\rho \sum_{k=1}^{N} V_{k,i} Y_k h_{s,k}} \right) + \overline{S}_{energy}, \quad (3)$$

$$\frac{\partial \left(\overline{\rho} \tilde{Y}_k \right)}{\partial t} + \frac{\partial \left(\overline{\rho} \tilde{u}_i \overline{Y}_k \right)}{\partial x_i} = \frac{\partial}{\partial x_i} \left[\overline{V_{k,i} Y_k} - \overline{\rho} \left(\widetilde{u_i Y_k} - \tilde{u}_i \tilde{Y}_k \right) \right] + \overline{S}_{species}$$
$$k = 1, N, \quad (4)$$

where the density, velocity, pressure, enthalpy, and mass fraction of species k are denoted respectively, by ρ, u, p, h_s, and Y_k. $V_{k,i}$ is the laminar diffusion coefficient of species k. The gradient diffusion assumption with the unitary Lewis number (Le = 1) is adopted for modeling the laminar diffusion term for multi-component turbulent flows in this paper, which has been widely used in the recent literature.[43–45] τ_{ij} stands for stress tensor. The source terms $\overline{S}_{mass}$, $\overline{S}_{momentum}$, $\overline{S}_{energy}$, and $\overline{S}_{species}$ stand for the interaction effect between gas flow field and spray field. These source terms stand for the mass transfer into gas fields due to the evaporation of liquid droplets, the momentum transfer between phases, the energy transfer due to phases and chemical reactions, and the transfer of species, respectively.

Table I shows the critical temperature as well as the critical pressure of the involved substances in this paper. The pressure of the operating conditions used in this paper is only 1.2 MPa, which is below the critical region for all the substances involved. Therefore, the equation of state for the ideal gas law is used in this paper to relate the pressure, temperature, and density of fluids. The equation is expressed as $pV = nRT$, where p is the pressure of the gas, V is the volume, n is the number of moles of gas, R is the universal gas constant, and T is the absolute temperature. For compressible gases, the density of the gas mixture changes with the oscillation of the pressure in the combustion chamber, which is essential for the simulation of unstable combustion processes. On the other hand, the speed of sound of the gas mixture also changes significantly with the temperature of the gas and, therefore, affects the acoustic propagation process. The gas density and sound speed of the ideal gas hypothesis as a function of temperature are drawn in Fig. 1, which are also compared to the measured data given by the NIST website. Since oxygen, carbon dioxide, and water vapor occupy almost the entire volume of the combustion chamber, their thermophysical properties within the temperature range of interest are provided. The n-dodecane in the combustion chamber is mainly in the form of liquid droplets. Also, the temperature range openly available on the NIST website is only available up to 658 K, lacking a valid comparison under vapor conditions. Therefore, the thermophysical properties of fuel vapors are not being compared here. Based on our results, we observe that assuming an ideal gas provides a good approximation for thermophysical properties such as density and speed of sound at operating pressure. Therefore, it is reasonable to use the ideal gas assumption for subcritical conditions in this paper. The thermophysical models of the gas phase used in this paper have

TABLE I. Critical temperatures and pressures for these substances.

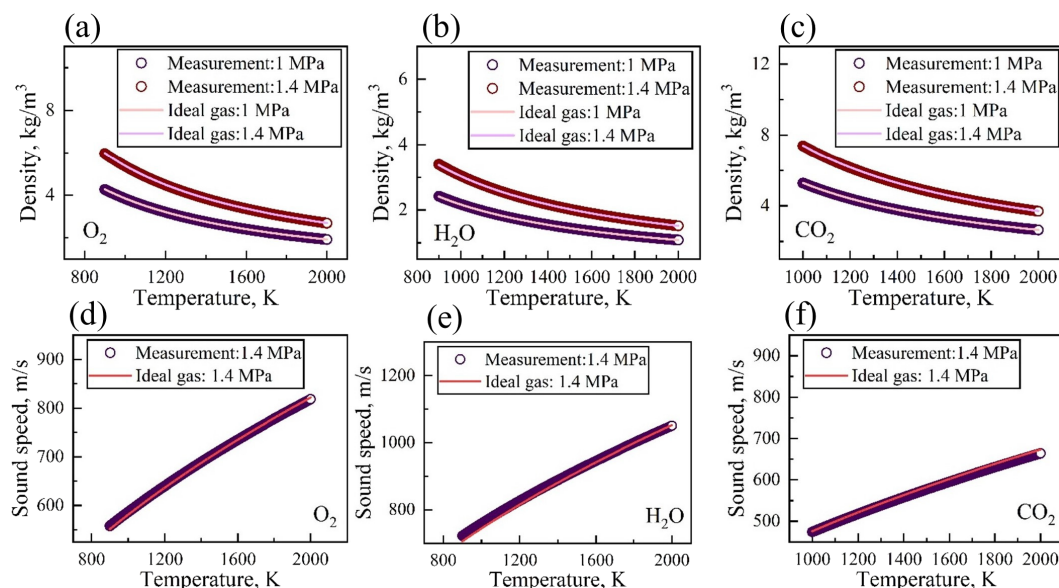| Substance	Critical temperature (K)	Critical pressure (MPa)
n-dodecane	658.2	1.8
Oxygen	154.6	5.04
Water	647.3	22.06
Carbon dioxide	304.2	7.38
Nitrogen	126.2	3.39

FIG. 1. Comparisons of thermophysical properties of gas-phases between the calculated results (solid line) and NIST data (circle line). Density: (a) oxygen, (b) water vapor, and (c) carbon dioxide. Sound speed: (d) oxygen, (e) water vapor, and (f) carbon dioxide.

been described in detail in our previous papers in 2022,[46] in which Janaf thermophysical model and the Sutherland transport model were used.

The atomization effect, breakup effect, evaporation rate, drag force, heat transfer, and the interaction between droplet and wall are briefly described by sub-models listed in Table II. The liquid evaporation boiling (LEB) model in OpenFOAM is used to simulate the evaporation of liquid droplets. The LEB model is a mass transfer model that takes into account both the diffusion and convection of vapor from the droplet surface. The LEB model also includes models for the heat transfer between the droplet and the gas phase, as well as for the change in droplet size due to evaporation. When the ambient pressure exceeds the saturated vapor pressure of the liquid, the non-equilibrium boiling model should be used. Conversely, if the ambient pressure is lower than the saturated vapor pressure of the liquid, the evaporation model should be employed. In particular, a simplified D^2-theory provides the evaporation rate under normal equilibrium evaporation in the LEB model. For a more detailed mathematical description of these spray sub-models, refer to the literature.[47] The partially stirred reactor (PaSR) sub-grid combustion model adopted in

this paper accounts for the interaction between the turbulence effect and finite rate chemical reactions and has been widely utilized to simulate rocket combustion.[46,48,49]

B. Numerical details

1. Physical model

As shown in Fig. 2, the computational configuration for this paper is a single-element coaxial liquid rocket engine with an oxidizer post, a combustion chamber, and a choked nozzle. Hydrogen peroxide at a concentration of 90% is used as an oxidizer, which is dissociated into high-temperature 58% water vapor and 42% oxygen (by weight) at 1030 K before entering the burner. Kerosene droplet at room temperature enters the combustion chamber coaxially with the oxidizer at the dump plane ($x = 0$). The simplified spraying approach is a gas-centered, liquid swirl injector element. The calculation parameters

TABLE II. Spray sub-models.

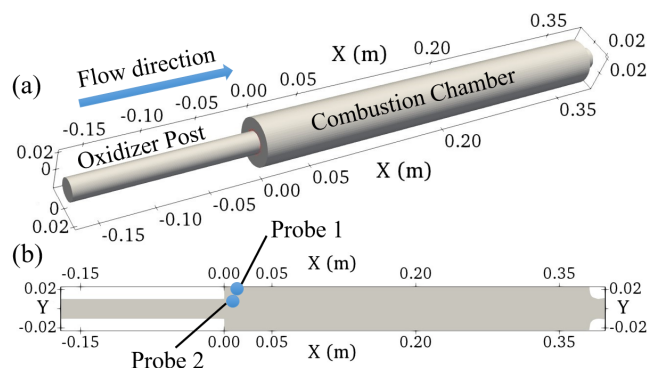| Models	Name
Atomization	None
Secondary breakup	ReitzDiwakar
Evaporation	Liquid evaporation boil
Heat transfer	RanzMarshall
Wall interaction	Rebound
Drag force	Sphere

FIG. 2. (a) Overview of the computational domain. (b) The $x - y$ plane ($z = 0$) marked by the monitoring points.

TABLE III. Computational conditions.

Case	1	2	3	4	5	6	7
Equivalence ratio	1.5	1.3	1.1	1.0	0.9	0.7	0.5
Kerosene mass flow rate, g/s	77	67	57	52	47	37	26
Kerosene temperature, K				300			
Uniform kerosene diameter, μm				50			
Cone angle				90°			
Parcels per seconds				20 000 000			
Oxidizer mass flow rate, g/s				231			
Oxidizer temperature, K				1030			
Operating pressure, MPa				1.2			

were sourced from experimental research conducted at Purdue University.[50] The time traces of pressure, velocity, temperature, mass fraction of oxygen, and mass fraction of kerosene are monitored by probe 1 and probe 2. The locations of the monitoring points are shown in Fig. 2(b). Probe 1 (0.0127, 0.022, and 0 m) is located near the wall and the pressure antinode of the first-order acoustic mode of the combustion chamber. Probe 2 (0.01, 0.01, and 0 m) is located at the initial shear layer, where the vortex flows through. The frequency corresponding to the highest peaks of its velocity spectrum is identified as the vortex-shedding frequency.[16]

To investigate the transition process of combustion stability, the equivalence ratio is used as the research variable in this paper. It is well known that the equivalence ratio has a significant impact on combustion instability. The mass flow rate of the kerosene is systematically altered because the mass flow rate of the kerosene is very small compared to the total mass flow rate of the oxidizer and, therefore, has little effect on the cold flow field. Table III summarizes the calculated conditions used in this paper. The range of values for the equivalence ratio decreases gradually from 1.5 to 0.5. The assumption of a uniform droplet size distribution was adopted, where a size of 50 μm was the

TABLE IV. Chemical kinetic mechanism.

Reactions	A, s^{-1}	E_a, J/(kg mol)	b	c	d
$C_{12}H_{26} + 18.5O_2 \rightarrow 12CO_2 + H_2O$	$5e^8$	15780	0	0.25	1.5

common intermediate diameter for engine operating conditions.[51] Subcritical turbulent combustion was established at an operating pressure of 1.2 MPa in the combustion chamber, which is below the critical pressure of kerosene (2.3 MPa).

2. Chemical kinetic mechanism

Liquid kerosene, as a mixture, is a hydrocarbon fuel commonly used in the rocket propulsion community. In turbulent combustion simulations of kerosene, n-dodecane ($C_{12}H_{26}$) is used as an alternative fuel in this paper because of its accessible physicochemical properties and chemical kinetic mechanism.[42] The single-step global chemical reaction mechanism is considered here to balance computational accuracy and efficiency, which has already proven to be effective in simulating combustion instability in rocket engines.[52–54] The rate of chemical reactions was calculated using the following equations:

$$k_f = AT^b \exp\left(-\frac{E_a}{RT}\right), \tag{5}$$

$$\dot{\omega}_k = \frac{d[product]}{dt} = -k_f [fuel]^c [oxidizer]^d, \tag{6}$$

where k_f, A, b, and E_a are forward reaction coefficient, pre-exponential factor, temperature exponent, and activation energy, respectively. The detailed chemical reaction mechanism and related parameters are shown in Table IV.

Using CHEMKIN, the adiabatic combustion temperatures and main product species (H_2O and CO_2) of $C_{12}H_{26}$-1-Reaction (a global chemical mechanism) and $C_{12}H_{26}$-269-Reactions (54 species, a skeletal mechanism proposed by Yao et al.[55]) were calculated at an initial temperature of 1200 K and pressure of 1.2 MPa. Figure 3 shows the results, which indicate that the simulation results for global chemical reaction kinetics are worse when the equivalent ratio is greater than 1.0 compared to those obtained using the skeletal mechanism. In fact, it is difficult for single-step chemical reactions to work effectively across a wide range of equivalence ratios. However, in the fuel-lean conditions that are of greater interest in this paper, the results are similar to those obtained from detailed chemical reaction kinetics. More complex pressure oscillations (beyond simple period −1) occur under fuel-lean conditions, as we will see later. Therefore, in order to balance calculation accuracy and efficiency, we have chosen to continue using the single-step chemical reaction mechanism for subsequent calculations.
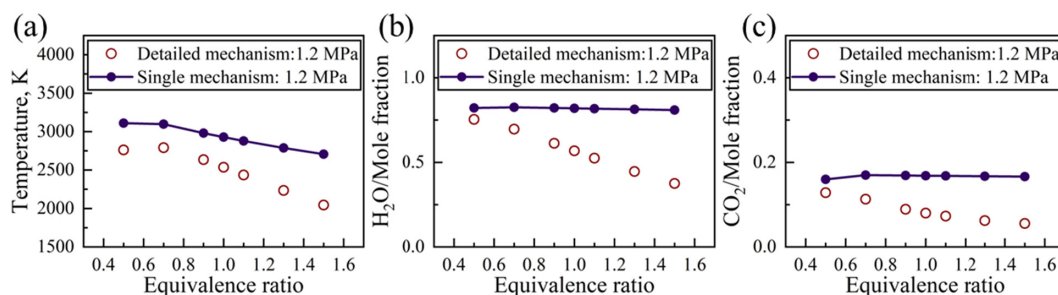
FIG. 3. Comparisons between the global single-step chemical mechanism and the skeletal mechanism proposed by Yao et al.,[55] in terms of adiabatic combustion temperature, H_2O mole fraction and CO_2 mole fraction as functions of equivalence ratio at p = 1.2 MPa and $T_{initial}$ = 1200 K.

3. Boundary conditions and initial conditions

For the inlet of the oxidizer post, the combination of constant mass flow rate and zero-pressure gradient boundary conditions is adopted to represent the oxidizer flow through the post and the complete acoustic reflection conditions at the inlet. This is because the choked oxidizer slots are also attached to the front of the oxidizer post in the experimental setup, which is not included in the computational domain instead the pressure boundary condition with zero-gradient (rigid acoustic boundary). The exit pressure boundary condition is set to wave transmissive condition, which ensures the acoustic choked nozzle condition. The walls are set to be no-slip, impermeable, as well as adiabatic. The spray conditions are set to be cone injection model, where the cone angle is set as 90°. The constant mass flow rate condition of the fuel droplet is set here.

The initial conditions for calculating the computational domain include static nitrogen at a pressure of 1.2 MPa and temperature of 2000 K. Herein, the operating conditions can be quickly established.

C. Numerical procedure

The numerical framework developed in this work was solved numerically using the finite volume method (FVM) based on the open-source platform OpenFOAM-6 with a modified version of the sprayFOAM solver. The PIMPLE algorithm was used to deal with the coupling between pressure and velocity. The operating condition simulated in this paper is a model liquid rocket engine with a high Reynolds number. Therefore, the Eulerian implicit scheme has been adopted to balance computational efficiency and accuracy, which has also been employed in recent numerical studies.[46,56,57] The second-order central difference scheme was used to discretize the convection term and the diffusion term. An adjustable time step method was used to avoid numerical instability, and the corresponding CFL number was set to 0.6. The calculation time step is approximately 8×10^{-8} s.

III. VALIDATION OF NUMERICAL FRAMEWORK

In this section, two benchmark flows for the validation of the numerical framework are discussed. The self-excited combustion instability of a hydrogen peroxide/kerosene engine working at critical pressure conditions is simulated in the first benchmark case, which is used to validate the turbulence effects and the chemical reaction mechanism of this paper. The second benchmark case simulates the vaporizing spray process of n-dodecane regardless of chemical reactions to validate the two-phase interaction and evaporation model.

A. Benchmark 1

The experiment used for verification comprised a single-element liquid rocket engine, designed at Purdue University.[50] A gas-central, liquid-swirl coaxial injector element was selected to couple the combustion chamber and choked nozzle, as shown in Fig. 4. Liquid kerosene was used as a liquid-phase fuel while a hot mixture at a temperature of 1030 K including 58% water vapor and 42% oxygen by weight was used as a gas-phase oxidizer. The design operating pressure of the combustion chamber was 2.4 MPa, which is close to the critical pressure of 2.3 MPa for kerosene. The benchmark experiment was conducted at a nominal mixture ratio (O/F) of about 6.3. The total mass flow rate was 0.535 kg/s. Further details can be found in the literature.[50] The variable length of the combustion chamber was discretely
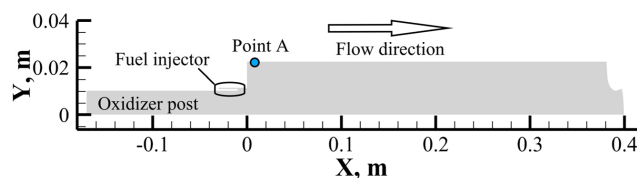

FIG. 4. Schematic diagram of the axisymmetric computational domain in Benchmark 1.

varied from 25.4 to 88.9 cm. When the length of the combustion chamber was fixed at 38.1 cm, high amplitude pressure oscillations were experimentally observed. Unstable combustion occurred at the frequency of 1502 Hz, which is the first-order acoustic frequency of the combustion chamber.

The n-dodecane ($C_{12}H_{26}$) was used as an alternative fuel to replace the highly complicated mixture of JP-8 fuel. To enable further simplification of the analysis, the fuel was modeled as a vapor state represented by the perfect gas assumption, thereby neglecting the interaction of the gas and liquid phases. The assumption of an axisymmetric calculation domain was also adopted. The feasibility of neglecting gas–liquid interactions and the axisymmetric calculations are discussed in detail in Ref. 52, which is not the main focus of this paper. The pressure trace in the combustion chamber was monitored at point A (0.0127, 0.022, and 0 m) near the antinode of first-order acoustic mode. It is also worth noting that the temperature of the fuel vapor was uncertain, as the ideal gas assumption was adopted. Therefore, the temperature of kerosene vapor was parameterized for this study with all three operating conditions above the critical temperature. The sensitivity of the LES results to the grid resolution has been discussed earlier in numerical simulations by the authors,[46] where the computational domain is the same as in Fig. 4.

Figure 5 shows the time evolution of pressure at different temperatures of kerosene vapor and the results of the fast Fourier transform (FFT) at the time interval of 35 to 50 ms. The experimentally observed high amplitude instability is reproduced by the numerical simulation results. Table V further compares the dominant frequencies and amplitudes with the experimental measurements under three conditions with different kerosene vapor temperatures. The calculated results for the three dominant frequencies are consistent, with an error of 2% from the experimental results. The relatively small frequency errors indicate that the numerical framework is able to solve the acoustic modes of the system very well. However, the errors in the amplitudes corresponding to the three operating conditions are 39.7%, 25.2%, and 17.2%, respectively. The prediction error of the amplitude can be attributed to the simplification of the gas–liquid interaction effect and the assumption of axisymmetric computation neglecting the vortex-stretching effect. In summary, the numerical simulation results for Benchmark 1 validate the numerical framework for turbulent combustion calculations of kerosene and the ability to capture self-excited instabilities.

B. Benchmark 2

The experimental setup for Benchmark 2 involved ECN Spray A cases[42] designed by Sandia National Laboratory. The liquid fuel n-dodecane was injected from a single hole into a constant volume chamber. The high pressure (6 MPa) and high temperature (900 K)
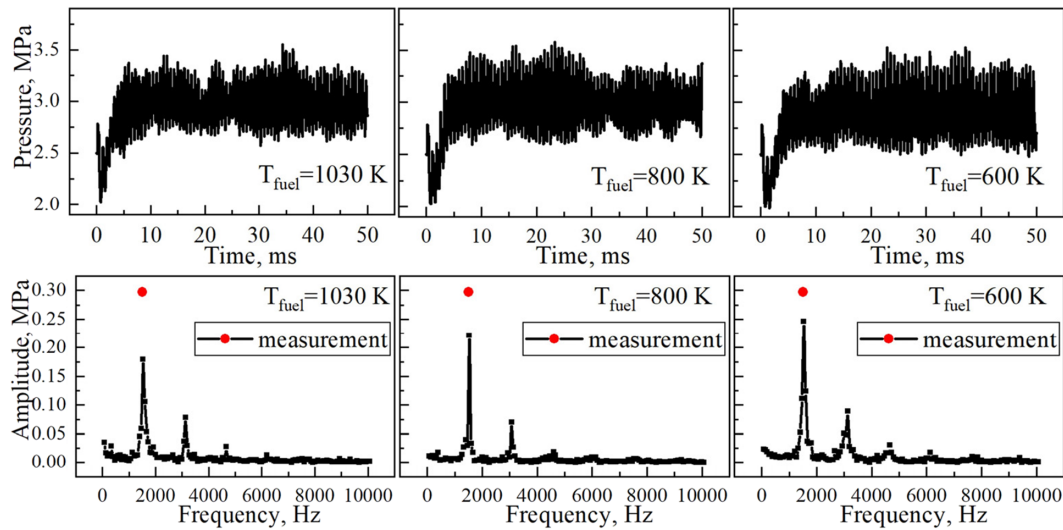
FIG. 5. Pressure traces and corresponding FFT results monitored at point A. The instability frequencies and amplitudes measured by the experiment were 1502 Hz and 297 kPa, respectively.[58]

TABLE V. Comparison of dominant frequencies and amplitudes with experimental measurements in Benchmark 1.

Benchmark 1	Experiment	1030 K	800 K	600 K
Frequency, Hz	1502	1533	1533	1533
Amplitude, kPa	297	179	222	246

FIG. 6. Liquid and vapor penetration length in non-reacting spray A case; solid lines: LES results; broken lines: experimental measurements.[42]

mixture filled the ambient chamber, including 89.71% nitrogen, 3.77% water vapor, and 6.52% carbon dioxide by weight. The diameter of the injector hole was small (9×10^{-5} m), and the injection pressure was high (150 MPa), which facilitated the rapid atomization of kerosene as well as its evaporation. For a more detailed presentation of the experiment, reference can be made to Ref. 43. In this study, the numerical calculations are based on a three-dimensional cube where the cross section is a square of 70×70 mm and the height is 180 mm. The grid is refined near the fuel injection nozzle, where the refined area is also a cube with sides of 16×16 mm and a height of 78 mm. The minimum grid volume in the entire calculation area is 1.25×10^{-10} m^3, while the maximum grid volume is 4.4×10^{-10} m^3. The total number of hexahedral meshes is 2.2×10^6, which satisfies the need for grid-independence. The adjustable calculation time step method is used, where the maximum value of the CFL number is set to 0.25. The time step of the solution is about 5×10^{-7} s. The time evolutions of the liquid as well as the vapor from the evaporation process during the time interval of 1.5 ms after the start of the injection are the focus.

Figure 6 shows a comparison of the experimental measurements with the results of the large eddy simulation. Vapor, as well as liquid penetration length, was used as post-processing variables. The liquid and vapor penetration length are defined as the distance from the nozzle to the furthest axial location, where both the liquid volume and the vapor mass fraction are 0.1%.[43] The numerical simulation results for both the liquid penetration length and the vapor penetration length are in good agreement with the experimental measurements for an
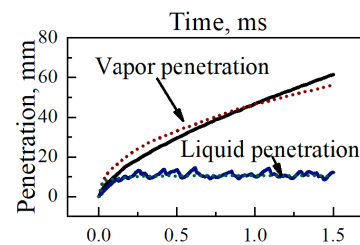
injection time interval between 0 and 1.5 ms. The results of Benchmark 2 verify the validation of the Eulerian–Lagrangian framework together with the spray sub-models used in this paper.

IV. RESULTS AND DISCUSSION
A. Verification of grid independence

To improve the quality of the numerical simulation, two different meshes were used to verify the grid-independence. Mesh 1 consisted of 4.1×10^6 hexahedral cells, while mesh 2 was enhanced in the longitudinal direction and contained a total of 5.2×10^6 hexahedral cells. The smallest radial grid size was 60 μm, located at the wall and shear layers. Figure 7 compares the time traces of the pressure and the results of the fast Fourier transform (FFT) at time intervals between 15 and 30 ms in case 1. High amplitude instabilities were captured by both meshes. The pressure rise stage as well as the high amplitude instability stage of both grids is well matched. The calculation results of the two meshes are compared in terms of the unstable frequencies and the amplitudes using FFT technology. On the one hand, the characteristics of the oscillations are well captured, although there is still some difference in their amplitude. On the other hand, each operating condition in mesh 1 consumed approximately 49 000 CPU core hours in a 50 ms calculation time. Therefore, to balance computational
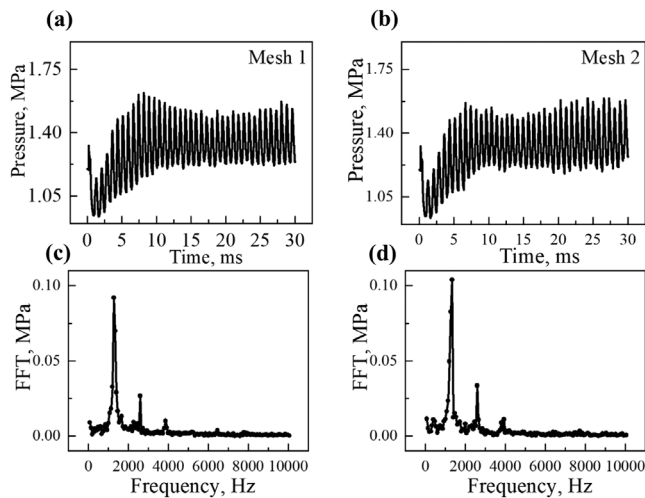
FIG. 7. Time evolution of the pressure (a) and (b) monitored at probe 1 for different meshes and corresponding FFT results (c) and (d); mesh 1: 4.1×10^6 hexahedral cells; mesh 2: 5.2×10^6 hexahedral cells.

efficiency as well as computational accuracy, mesh 1 was adopted as the subsequent computational mesh for this paper.

B. Thermoacoustic instability: Period-1 oscillation

The first insight is the spatial distribution of the flow field. Figure 8 shows a snapshot of the instantaneous combustion flow field in case

1 for $t = 45$ ms. Vortices are formed at the shear layer downstream of the dump plane, due to the interaction between the high-velocity flow and the low-velocity flow. The flame is stabilized in the recirculation zone. The vortex structure has a significant effect on the heat release distribution like gas-fueled propulsion systems and even controls the flame structure in such liquid-fueled spray combustion systems, which can be attributed to the rapid evaporation of liquid droplets in the recirculation region and, thus, their accumulation downstream of the dump plane. When acoustic oscillations are introduced, the interactions between subsystems, such as vortex dynamics, combustion, and species, become more complex. This paper aims to reveal the evolution of the underlying complex pressure oscillations for these subsystems as well as provide a more important insight into physical understanding.

Figure 9 illustrates the detailed dynamics of the pressure oscillations in case 1. Band-pass filtering techniques as well as phase space reconstruction techniques are employed to understand the linear and non-linear behavior of the pressure oscillation, respectively. The raw pressure traces are artificially segmented into four-time segments: the rise in mean pressure due to the ignition process colored black, the transition stage colored red, the pressure oscillation stage colored blue, and the decay stage of the pressure oscillation colored green. During the onset of thermoacoustic instability, the frequency characteristics of the pressure consist of the dominant mode at 1300 Hz along with higher-order modes, where 1300 Hz is identified by the theoretical analysis as the first-order longitudinal (1L) acoustic frequency of the combustion chamber. As the pressure evolves in time, the amplitude corresponding to the 1L acoustic mode is always greater than the higher-order harmonics. Considering that the bandpass filtering
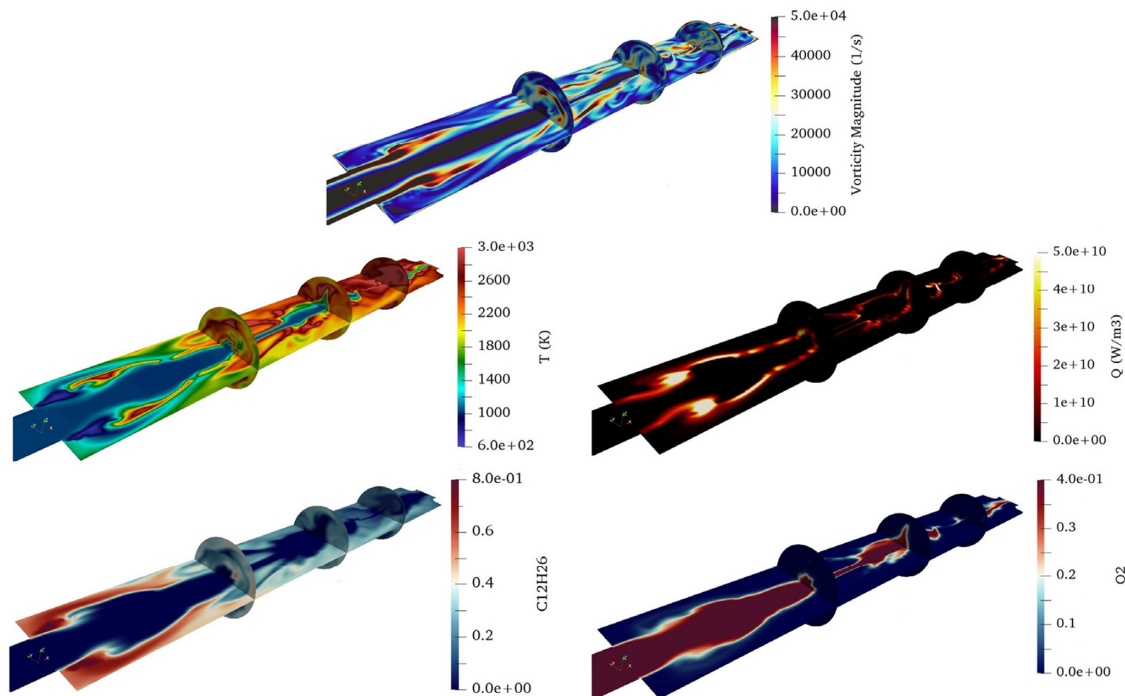

FIG. 8. Instantaneous snapshots of the flow field: vorticity magnitude (1/s), temperature (K), heat release rate (W/m^3), mass fraction of kerosene vapor, and mass fraction of oxygen in case 1.
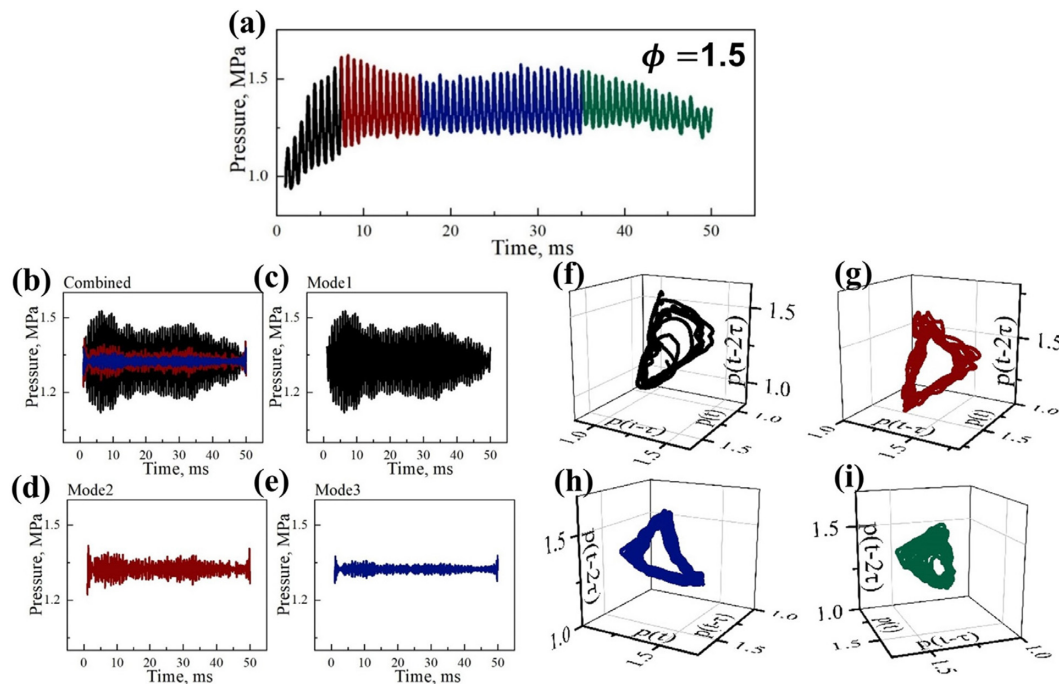
FIG. 9. (a) Time evolution of pressure signals monitored at probe 1; (b)–(e) The filtered time evolution of pressure corresponding to the first three orders of acoustic mode. Mode 1: 1300 Hz. Mode 2: 2600 Hz. Mode 3: 3900 Hz; (f)–(i) Reconstructed phase portraits for four different time segments. The time delay τ is equal to one-quarter of the oscillation period.

technique is a linear tool, the phase space reconstruction technique is used to analyze the non-linear states of the dynamics. In the first segment (black), the trajectory of the phase diagram initially starts at a single point and gradually spirals outward, indicating period-1 (P1) oscillations during the initial growth. In the second (red) and third segments (blue), the phase trajectory in the embedding space is tensed into a single-loop structure, also indicating P1 oscillations. In the fourth segment (green), the phase trajectory starts with existing P1 oscillations and gradually spirals down toward the center of the embedding space. It is noteworthy that the geometry of the phase space trajectory at this point remains a single-loop structure, indicating P1 oscillations in the pressure decay segment. Although the dynamical characteristics of pressure are well understood, the simultaneous examination of subsystems, such as combustion as well as vortex dynamics, is still necessary to obtain a further understanding of the driving mechanism of combustion instability.

The vortex-related dynamics were monitored at probe 2, where the vortex flowed through. Figure 10 shows the time series of velocities in the y-direction and the results of the FFT for three different time segments. The dominant frequency of the flow oscillation in the first segment between 1 and 10 ms is 1222 Hz, indicating that the frequency of vortex shedding is also 1222 Hz. During the second and third segments, the frequency of vortex shedding was identified as 1300 and 1243 Hz, respectively. Due to the P1 thermoacoustic oscillations at the second segment, the temperature and speed of sound in the combustion chamber are increased, thus leading to higher acoustic frequencies. In summary, the dominant frequency of vortex shedding during the P1 thermoacoustic oscillation is the first-order longitudinal (1L)

acoustic frequency, both in the initial, self-sustaining, and decaying phases of the oscillation. The complexity of thermoacoustic oscillations indicates that the dynamics are beyond simple period-1, which may manifest in the non-sinusoidal behavior of the dominant mode.

To obtain the dynamical response of the combustion subsystem during P1 oscillations, the time series of kerosene mass fraction, temperature, as well as oxygen mass fraction are plotted in Fig. 11. The corresponding phase portraits during the P1 oscillation are also reconstructed to reveal the non-linear state of the P1 oscillation. We observe that the amplitude of the subsystem response shows a significant variation with time. The amplitudes of these subsystems were significantly reduced during the initial phase and the decay phase of the oscillation. During the P1 oscillation at the time interval between 20 and 30 ms, a clear repeating pattern of phase portraits was observed, showing a stretched trefoil-knot-like structure. This structure is quite different from the phase portraits of pressure oscillations, which depict a single-loop structure. During the P1 thermoacoustic instability, there is a periodic raising of the temperature as well as the mass fraction of the species at the shear layer due to the high amplitude acoustic waves, which in turn leads to the steepening of the compression wave front into a combustion steep-fronted wave.

C. Intermittency route to period-2 oscillation

Changing the global equivalence ratio affects the fuel-to-oxidizer ratio of the mixture throughout the combustion chamber, which in turn affects the local equivalence ratios at different points. The local equivalence ratio is important because it affects the combustion
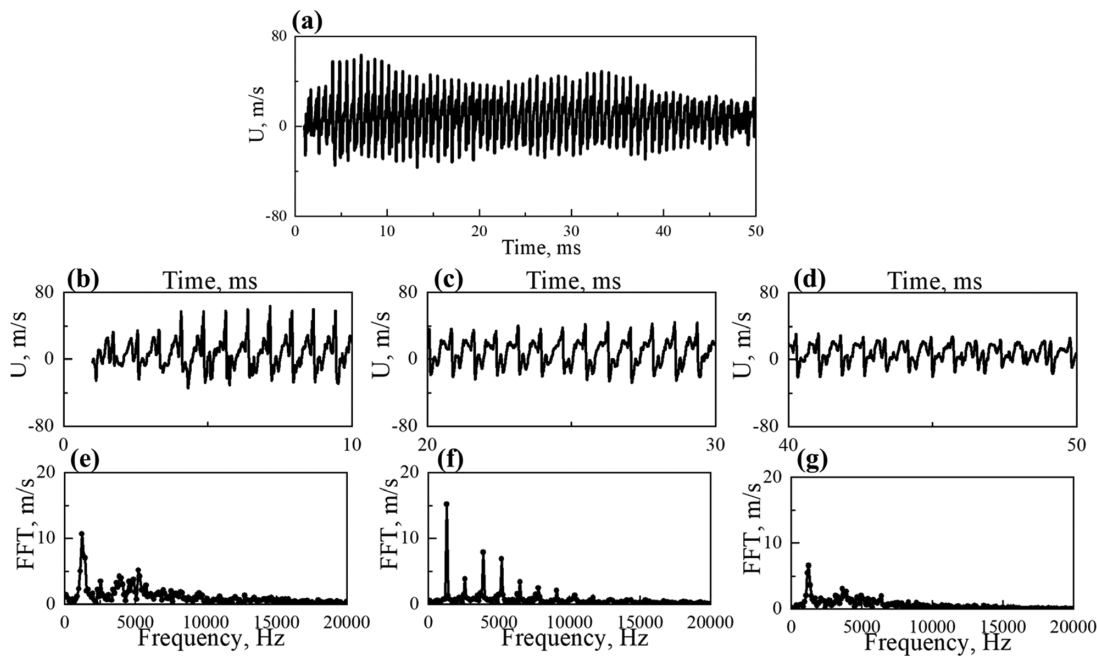
FIG. 10. (a) Time evolution of velocity in the y direction monitored at probe 2; (b)–(d) Enlarged time series; and (e)–(g) corresponding FFT results.
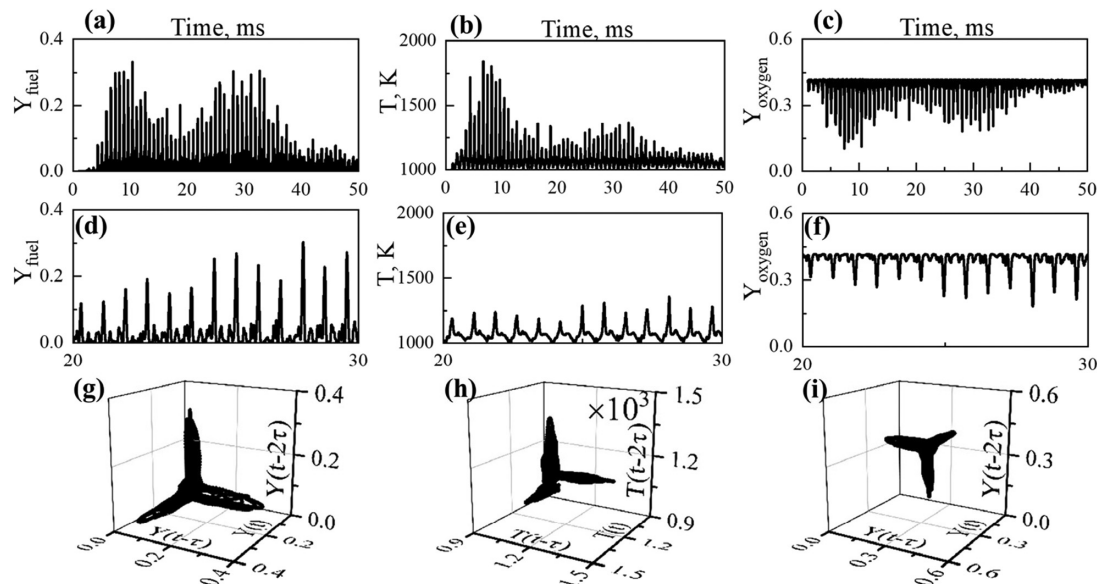

FIG. 11. Time series of mass fraction of fuel vapor (a), temperature (b), and mass fraction of oxygen (c) monitored at probe 2; enlarged time series during period-1 (P1) oscillation (d)–(f); and corresponding reconstructed phase portraits (g)–(i) during P1 oscillation.

characteristics at each point, even if the overall diffusion flame still occurs at a local equivalence ratio of 1. This paper is focused on the effect of global equivalence ratios on thermoacoustic instability. However, the bifurcation behavior of the system transitioning from the period-1 (P1) limit cycles to other non-linear states when the equivalence ratio is continuously reduced remains to be discussed. An in-depth understanding of how a system transitions to complex states is necessary as it can guide the design stage of the liquid rocket engines, paving the way for active control measures. This section shows the intermittency route ($1.3 \leq \phi \leq 0.9$) to period-2 (P2)

thermoacoustic instability ($\phi = 0.5$) by continuously reducing the equivalence ratio (ϕ). A transient mode switching between P1 and P2 was also observed under the equivalence ratio of 0.7 ($\phi = 0.7$). The time evolution from the intermittency route to P2 oscillations will be discussed in detail below in terms of pressure oscillations as well as vortex dynamics.

Figure 12 shows the time series of pressure, the corresponding filtered time series of the first three order acoustic modes, and the phase portraits in cases 2–5. Similar dynamic characteristics of the raw pressure traces are observed, which is called intermittency using the terminology of dynamical systems theory. During intermittency, periodic oscillations with high amplitude are followed by non-periodic oscillations with low amplitude. Although the physical time of the simulation is limited by computing resources to 50 ms, the intermittent changes in pressure amplitude are still well captured and can in turn provide a detailed explanation of the physical mechanisms. When the equivalence ratio is reduced from 1.3 to 0.9, the duration time of the periodic oscillations is reduced from 20 ms to about 10 ms. The results based on the filtered time series of the first three acoustic modes show that the amplitude of the pressure oscillations corresponding to the first-order acoustic modes is always greater than that of the higher

harmonics during periodic oscillations in intermittency. This also indicates that during the periodic oscillation in intermittency, the system dynamics are dominated by period-1 (P1) oscillations. In contrast, during non-periodic oscillations in intermittency, especially in cases 3–5, the amplitude of the pressure oscillations corresponding to the second-order acoustic modes is always non-negligible and even exceeds that of the first-order acoustic modes. This also indicates that the system dynamics are dominated by oscillations beyond simple P1. In the phase portraits of intermittent oscillations, the phase trajectory, as it evolves in time, first spirals outward into a single-loop structure and eventually invades the center of the embedded space as a solid region. Again, the results indicate that the system dynamics spontaneously transition between period-1 (P1) and aperiodic oscillations during intermittency.

It has been shown previously that the dynamical state of the system undergoes a transition from period-1 (P1) oscillations ($\phi = 1.5$) to intermittent oscillations ($1.3 \leq \phi \leq 0.9$) as the equivalence ratio is continuously reduced. However, a new dynamical state of period-2 (P2) oscillations were observed with a further decrease in the equivalence ratio. The understanding of the physical mechanisms underlying the intermittency route to P2 thermoacoustic instability
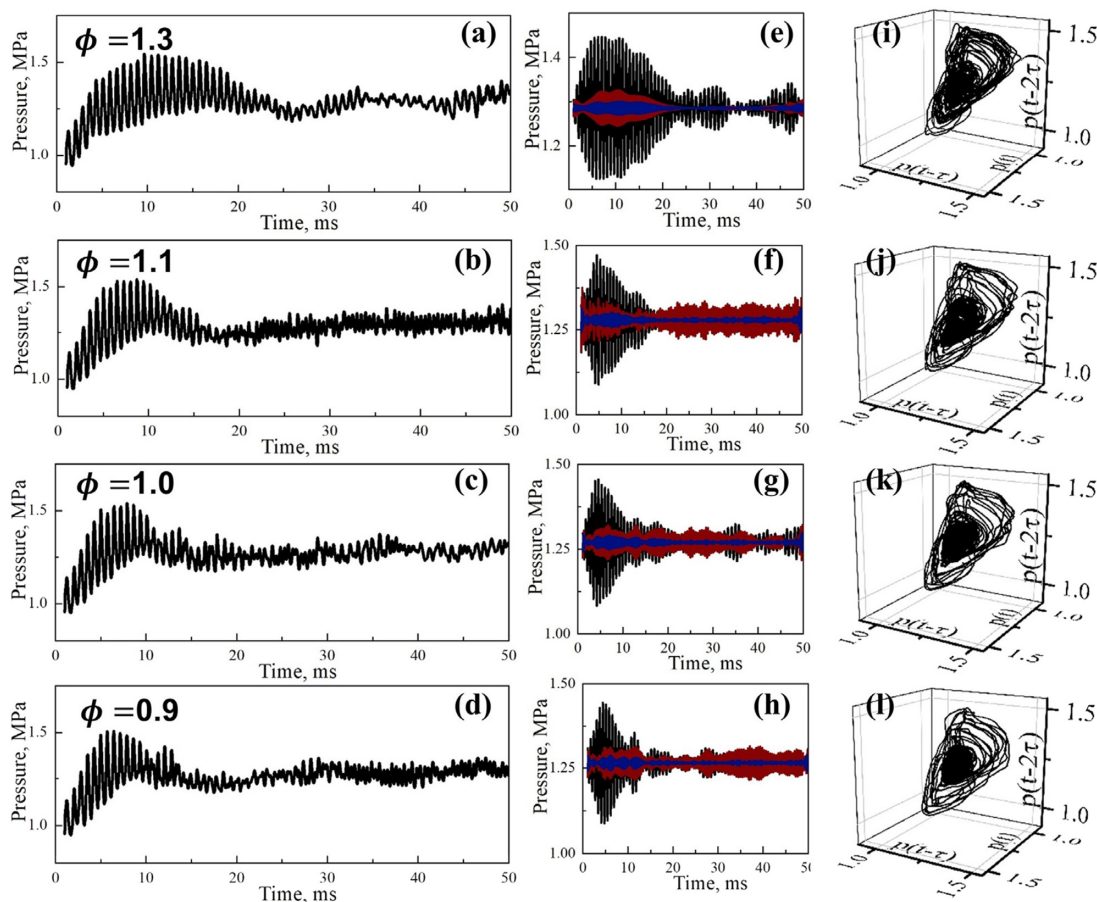

FIG. 12. Time series of pressures (a)–(d) undergoes intermittency in cases 2–5; filtered pressure traces corresponding to the first three orders of acoustic modes (e)–(h). Mode 1: black. Mode 2: red. Mode 3: blue; reconstructed phase portraits for time intervals between 1 and 50 ms (i)–(l).

is both academically interesting and engineeringly necessary. Figure 13 shows the raw time series of pressure in cases 6–7, the filtered results corresponding to the first two orders of acoustic modes in cases 6–7 and a magnified view of the waveform in case 7. At the beginning of the calculation time, the combustion chamber experiences a spontaneous increase in average pressure and oscillation amplitude. The filtered results based on the pressure also show that the oscillation amplitude of the first-order acoustic mode is much larger than that of the higher harmonics in the time interval from 1 to 10 ms, indicating the occurrence of a P1 thermoacoustic instability. As time evolves further, the waveform of the oscillation becomes more complex. In case 6, the filtered results show the alternating dominance of amplitudes corresponding to first-order (1L) acoustic modes and those corresponding to second-order (2L) acoustic modes, indicating the transitions between P1 oscillation dominance and P2 oscillation dominance. An enlarged view of the waveform for case 7 also provides details of the transition between P1 and P2 oscillations in the system dynamics, as well as the complete P2 oscillations over a time interval of 45 to 50 ms. The P1 oscillation will only produce a single set of peaks and troughs at each acoustic oscillation period from a waveform perspective. In contrast, the P2 oscillation produces two sets of peaks and troughs per oscillation period. In the waveform view, these are marked by circles as well as triangles, respectively.

In summary, the dynamic state of the system in liquid rocket engines is more complex than previously thought. On the one hand, the system exhibits intermittent and period-2 dynamic states in addition to the fixed-point or simple period-1 limit cycle in the parameter space of the equivalence ratios in this paper; on the other hand, the dynamical state of the system undergoes a series of possible transitions from the P1 state to the P2 state or from the P1 state to the

combustion noise state as time progresses. Although the dynamical state of the system in parameter space has been investigated, the intrinsic physical mechanisms remain the focus of attention in the rocket propulsion community, as these could pave the way for our future active control measures.

To investigate the transition process of the vortex dynamics in the intermittency, the velocity in the y-direction of case 2 is shown in Fig. 14. The three different time segments correspond to different dynamical states of the intermittent oscillation: the growth segment of the oscillation state, the decay segment of the oscillation state, and the non-periodic oscillation segment. The dominant frequencies of the vortex shedding for the three different time segments are 1222, 1299 Hz and a wideband spectrum range, respectively. The vortex shedding frequency remains the first-order (1L) acoustic frequency during the period portion of intermittency, implying that the system dynamics are dominated by the period-1 (P1) oscillation. By way of contrast, in the aperiodic portion of intermittency, the amplitude spectrum is broadband, encompassing a wide range of frequencies from 1000 to 5000 Hz with low amplitude.

The vortex dynamics of case 7 are shown to provide insight into the physical mechanism of period-n oscillations. As shown in Fig. 15, the velocity in the y-direction is monitored at probe 2. The FFT results corresponding to three different time segments are presented to provide an insight into the evolution of the vortex dynamics during the initial oscillation phase, the transition phase where the P1 oscillation gives way to the P2 oscillation, and finally the complete P2 oscillation segment. The dominant frequencies of vortex shedding in three different time segments are 1333 (1L), 2800 (2L), and 2900 Hz (2L), respectively. In the initial segment of the oscillation, the vortex shedding frequency remains at the frequency of the 1L acoustic mode. In the latter two segments, the vortex shedding frequency shifts from the 1L
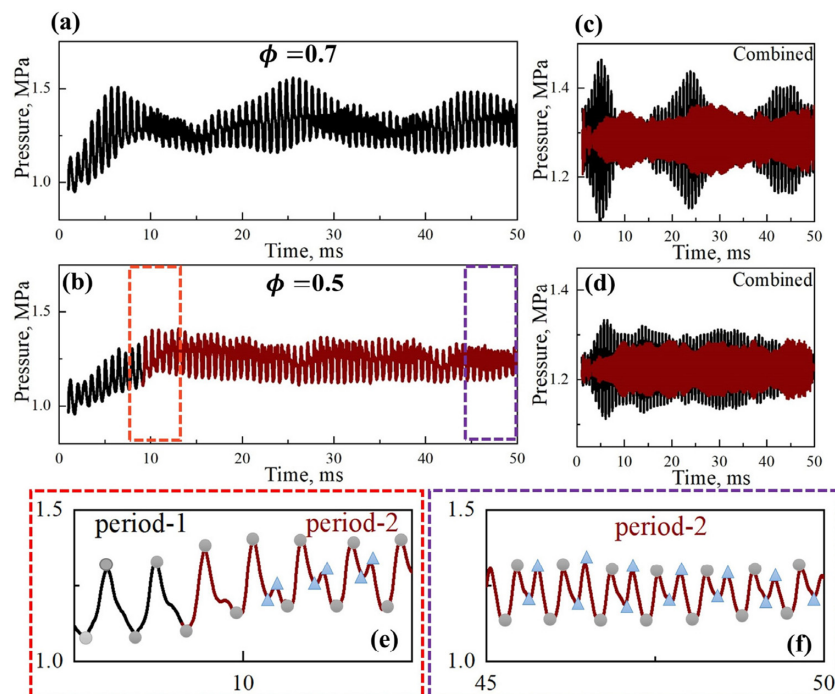

FIG. 13. Time series of pressure monitored at probe 1 in cases 6 and 7 (a) and (b); filtered pressure traces corresponding to the first two orders of acoustic modes (c) and (d). Mode 1 (1300 Hz): black. Mode 2 (2600 Hz): red; magnified view of the waveform during the transition between period-1 and period-2 oscillations in case 7 (e); magnified view of the waveform during period-2 thermoacoustic instability in case 7 (f). Every peak and trough labeled by a discrete colored marker.
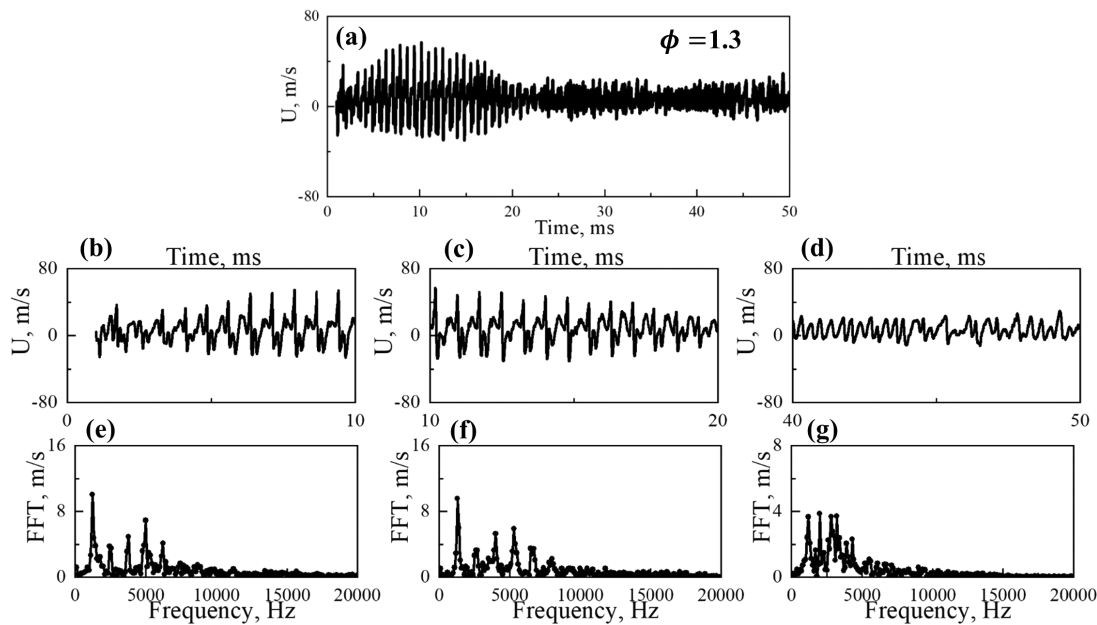
FIG. 14. (a) Time evolution of velocity in the y direction monitored at probe 2 in case 2; (b)–(d) Enlarged time series and (e)–(g) corresponding FFT results.

FIG. 15. (a) Time evolution of velocity in the y direction monitored at probe 2 in case 7; (b)–(d) Enlarged time series and (e)–(g) corresponding FFT results.
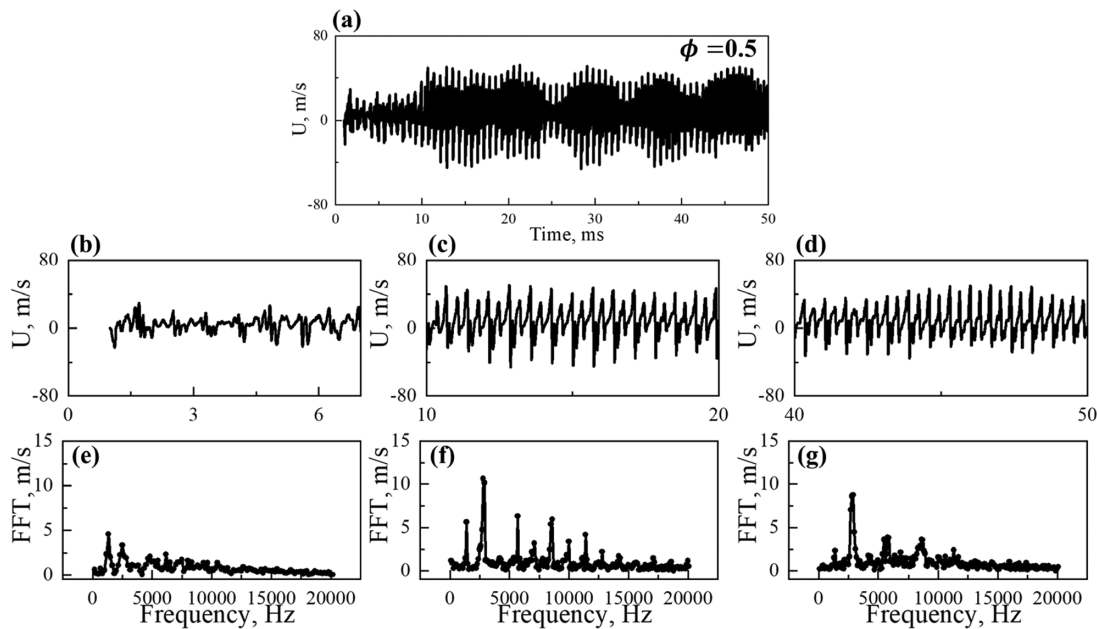
mode to the 2L mode. More interestingly, the amplitude of the velocity oscillations corresponding to the 1L acoustic mode remains high during the transition time segment. However, in the final time segment, the amplitude of the velocity oscillations corresponding to the first-

order acoustic mode almost disappears. In conclusion, in coaxial liquid rocket engines, different oscillation states can be attributed to different vortex-shedding modes, offering further insights into the relevance of vortex dynamics.

D. Synchronization process

The intermittency route to the period-2 thermoacoustic instability has been studied in Sec. IV C in terms of pressure oscillations as well as vortex dynamics evolution. However, combustion instability in LREs is a self-organizing process resulting from the mutual interaction between hydrodynamics, acoustics, and combustion subsystems. In recent years, growing evidence has shown that the phenomenon of mutual synchronization between these subsystems is responsible for the onset of combustion instability.[23] Synchronization is the phenomenon of rhythm matching between two or more coupled subsystems. This common phenomenon was first discovered by Huygens in the 17th century[1] when he observed that two pendulum clocks hung from the same beam were eventually locked into a state where the oscillations between them shared the same amplitude and frequency due to

the action of the beam. The coupling type and coupling strength between the oscillating subsystems determine the characteristics of synchronization. The thermoacoustic instability due to synchronization was first investigated in thermoacoustic systems by Pawar et al.[28] They concluded that the transition from the combustion noise state to the strong thermoacoustic instability state is through an intermittent phase synchronized (IPS) state (intermittency) and phase synchronized (PS) state (weak thermoacoustic instability state) and measuring the synchronization of acoustic pressure and unsteady heat release rate. In this regard, three different thermoacoustic states are discussed in this section using synchronization theory, i.e., period-1 oscillation, intermittency, and period-2 oscillation.

As the equivalence ratio decreases from fuel-rich to fuel-lean, three different stability regions are observed. Figure 16 demonstrates
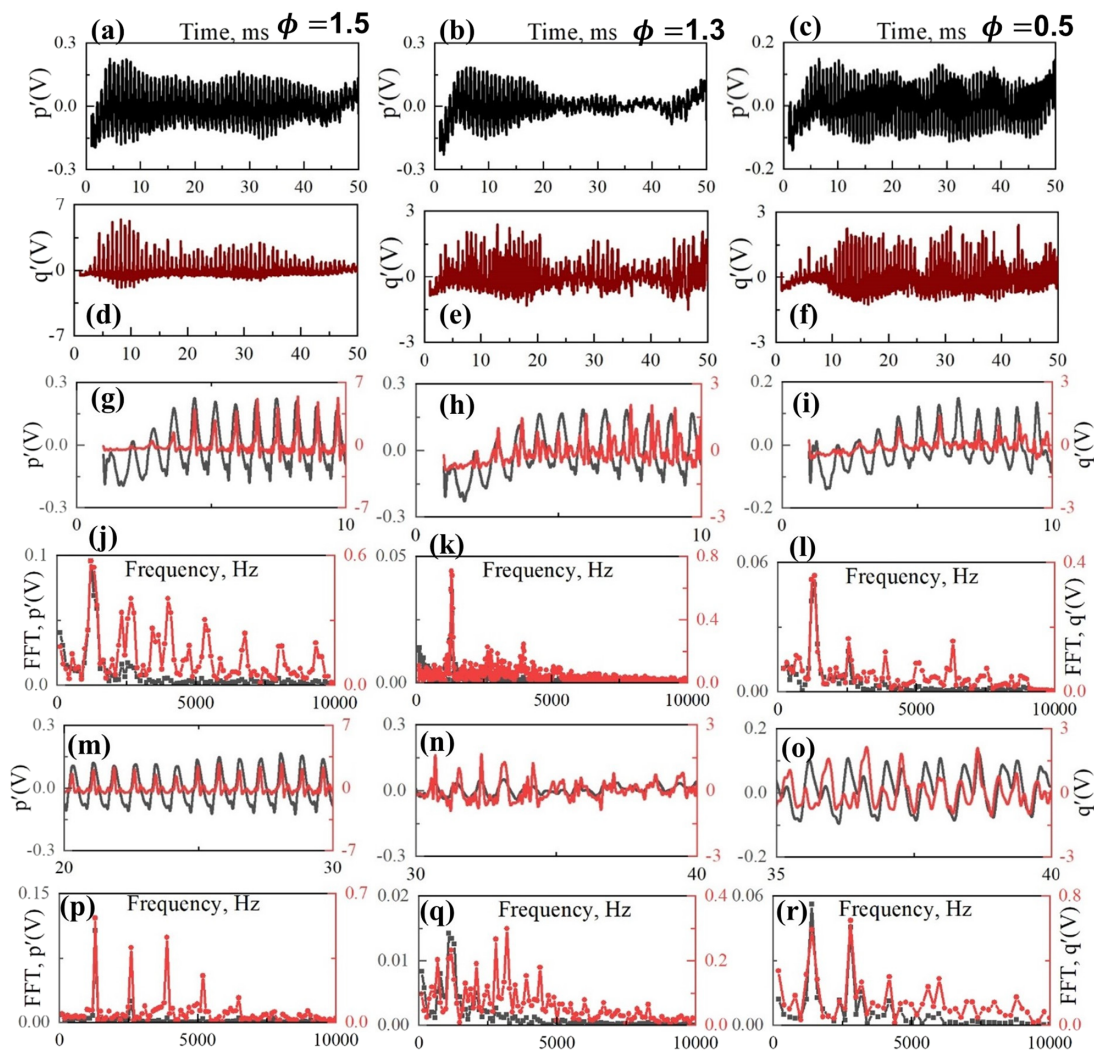

FIG. 16. Filtered time series of normalized pressure perturbation $p'(V)$ using a zero-phase-shift bandpass filter in the range of 100–10 000 Hz in cases 1, 2, and 7 (a)–(c) monitored at probe 2; filtered time series of normalized heat release rate feedback $q'(V)$ (d)–(f) monitored at probe 2; the overlapped time series of $p'(V)$ (black) and $q'(V)$ (red) during the state of period-1 oscillation (g) and (m), intermittency (h) and (n), and period-2 oscillation (i) and (o); the corresponding overlapped normalized amplitude spectrum of $p'(V)$ (black) and $q'(V)$ (red) during the state of period-1 oscillation (j) and (p), intermittency (k) and (q), and period-2 oscillation (l) and (r).

the synchronization of pressure and heat release rates in three different dynamical states. At an equivalence ratio of 1.5, high amplitude acoustic pressures are observed as well as heat release rates. As discussed earlier, at this point, the system dynamics are dominated by period-1 oscillations, whether in the growth phase, self-sustaining phase, or decay phase of the oscillation. At the beginning of the oscillation, in time intervals from 1 to 10 ms, we observe a transition from a phase-synchronized state (weak thermoacoustic instability) to an amplitude-synchronized state (strong thermoacoustic instability). The oscillation of the heat release rate is rapidly amplified from a low amplitude oscillatory state to a period-1 limit cycle state. The sharp dominant peaks of the FFT result in both states emerging from the pressure oscillations and the heat release rate oscillations. For both heat release rate oscillations and pressure oscillations, the sharp peaks in the FFT results and the overlapping dominant frequencies reveal the emergence of periodic oscillations in the dynamical system and the behavior of frequency locking under period-1 limit cycle oscillations.

At a much lower equivalence ratio condition ($\phi = 1.3$), we note typical intermittent dynamical characteristics, namely, the transition of flame dynamics from a period-1 oscillating state to a non-oscillating state with low amplitude. There is always a time lag between the pressure signal and the heat release rate signal during the period-1 oscillation, representing a weak thermoacoustic instability state at this point. In the non-oscillatory state, both the pressure oscillation and the heat release rate oscillation are non-periodic, indicating that the system is driven by turbulence-induced background noise. As shown in Figs. 16(k) and 16(e), during the initial oscillation segment, the dominant frequencies of the pressure signal as well as the heat release rate signal overlap around the first-order acoustic frequency, indicating the frequency-locked behavior of the period-1 oscillation. However, in the non-periodic segment of the intermittent oscillation, different dominant frequencies exist for the heat release signal and the acoustic pressure signal and the oscillation frequency of the heat release rate deviate from the acoustic frequency, indicating that these signals are not locked.

As the equivalence ratio decreases further ($\phi = 1.5$), we observe that the system dynamics eventually transition to a period-2 oscillation state, wherein the system dynamics grow initially through a period-1 oscillation pattern, and then transition to a period-2 oscillation. During the period-1 oscillations, the system dynamics are only in a state of phase synchronization (weak thermoacoustic instability). As time passes, both the pressure traces and the heat release rate traces appear to be characterized by period-2 oscillations, that is, the presence of two sets of peaks and troughs in each oscillation period. As shown

in Figs. 16(l) and 16(r), for the initial segment, the dominant frequencies of the two different signals are locked at first-order longitudinal (1L) frequencies. However, for the period-2 oscillation segment, the dominant frequency of the acoustic oscillation is the first-order longitudinal acoustic frequency, while higher-order harmonics coexist. The dominant frequency for the heat release rate, on the other hand, is the second-order harmonic frequency, while the first-order acoustic frequencies coexist. In summary, the dynamics of synchronization between the pressure traces and the heat release rate traces, in terms of phase-locking and frequency-locking in the time domain as well as in the frequency domain, provides further insight into the physical mechanisms underlying the intermittency route to the period-2 thermoacoustic instability.

E. Evidence from combustion flow fields

This section attempts to provide evidence for the intermittency route to period-2 oscillations and an underlying physical understanding from the cycle analysis of the combustion flow fields. Six moments of interest were selected for each cycle in the cycle analysis to highlight the unstable behavior of the different dynamical states corresponding to the period-1 oscillations (a), the non-oscillations in the intermittency (b), and the period-2 oscillations (c) shown in Fig. 17. In this section, the three-dimensional flow field was sliced and expanded in two dimensions, with the x-axis coordinates ranging from -1 to $10\,cm$ and $z = 0$. For an analysis of the mixing characteristics of the fuel as well as the oxidizer, the mixture fraction (Z) is defined as

$$Z = \frac{\nu_{st} Y_{fuel} - Y_{oxygen} + Y_{oxygen}^0}{\nu_{st} Y_{fuel}^0 + Y_{oxygen}^0}, \quad (7)$$

where $\nu_{st} = 3.5$, $Y_{fuel}^0 = 1$, and $Y_{oxygen}^0 = 0.42$. Y_{fuel} and Y_{oxygen} are the local mass fraction of fuel and oxygen, respectively. The stoichiometric mixture fraction is 0.107.

The first observation was carried out during period-1 oscillation in case 1. As shown in Fig. 18, a snapshot analysis within a cycle is performed, including vorticity magnitude, mixture fraction, and the heat release rate. The snapshot analysis starts at the time T1 when the pressure wave propagates to probe 1, also located at the head of the combustion chamber. Large-scale coherent structures are formed downstream of the dump plane subject to high-pressure waves. The interaction of spray combustion with acoustics under subcritical conditions has been less frequently discussed in laboratory-scale engines, compared to purely gaseous flames. The structure of the vortex
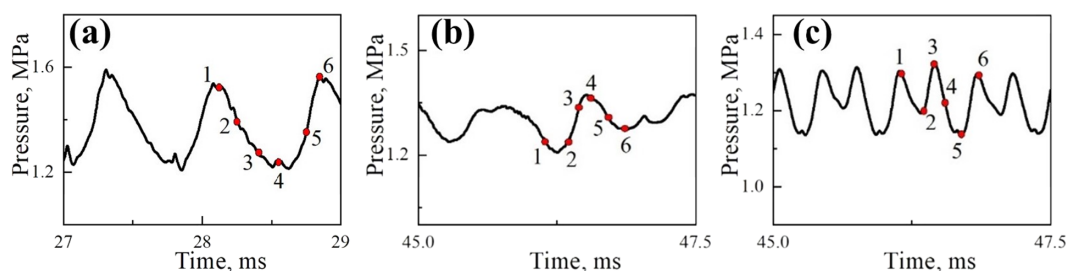

FIG. 17. Time series of the pressure of the cycle analysis monitored at probe 1. Case 1: (a), case 2: (b), case 7: (c). The marked red circles represent different moments of interest.
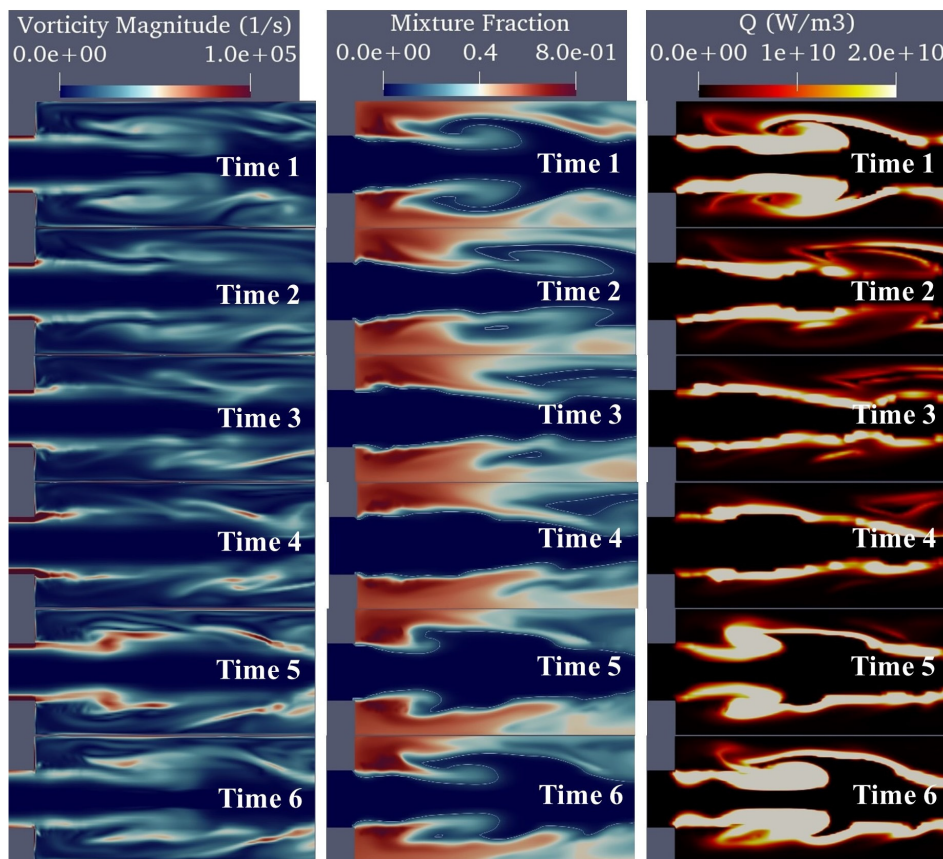
FIG. 18. Cycle snapshots for case 1 during the period-1 oscillation. Left image: vorticity magnitude (1/s). Middle image: mixture fraction. Right image: heat release rate (W/m^3).

dynamics is still a dominant factor, controlling the distribution of the mixture fraction as well as the flame structure, even when spray combustion and two-phase flow are present. In the presence of acoustic waves, the stoichiometric mixing fraction line (white lines, $Z = 0.107$) and the flame surface become more wrinkled, thus increasing the total amount of heat release. It can be qualitatively understood that the redistribution of fuel by vortex dynamics in the presence of acoustic waves can act as a potential driving mechanism for instability. However, under the operating conditions described in this paper, there are still similar conclusions to those for gaseous flames. This can be attributed to the fact that the high temperature of the oxidizer at 1030 K accelerates the evaporation process of the fuel droplet, thus allowing the turbulent diffusion effect to remain the dominant process in the combustion rate, while the evaporation effect is less influential. As the cycle progress to time 2, time 3, and time 4, the pressure near the dump plane decreases continuously during the propagation of the pressure wave downstream of the combustion chamber. The absence of significant wrinkling in either the mixture fraction line or the flame face also indicates the lack of combustion near the dump plane. Finally, the cycle evolves to the T5 and T6 moments and the pressure wave reaches its maximum near the dump plane at T6. The distribution of stoichiometric mixture fraction lines and heat release is still clearly wrinkled and forms a large coherent structure near the dump plane, representing that one cycle of oscillations is also completed in the combustion flow field at this point. In conclusion, when a period-1

thermoacoustic instability occurs, the various subsystems of the combustion flow field, such as mixture fraction, vortex dynamics, and heat release, all reach a synchronous state with the evolution of the pressure oscillations over time.

During the period-1 oscillations in intermittency, similar combustion flow field dynamics to those discussed in case 1 are observed and are, therefore, not repeated here. Figure 19 illustrates the time evolution of the combustion flow fields under non-periodic oscillations in intermittency. One of the most obvious differences is that no large-scale coherent structure is formed downstream of the dump plane. Both the stoichiometric mixture fraction lines and the flame surface are more continuous, and no obvious wrinkles are observed. It is noteworthy that we can still observe the evolutionary processes of vortex dynamics. Recall from the previous discussion that at this point, there is no frequency locking between the pressure oscillations, vortex dynamics, and heat release oscillations. The flame still exists to oscillate in its intrinsic dynamical mode.

Figure 20 illustrates the results of the cycle analysis of the combustion flow fields undergoing period-2 oscillations in case 7. The mixture fraction is significantly reduced in the recirculation zone because the global equivalence ratio of case 2 is the lowest. The basic feature of period-2 oscillations is the presence of two different sets of peaks and troughs within a single acoustic oscillation period, which means that the initial shear layer is excited by two sets of high-pressure waves. At T1 and T3, the high-pressure waves pass through the initial shear layer
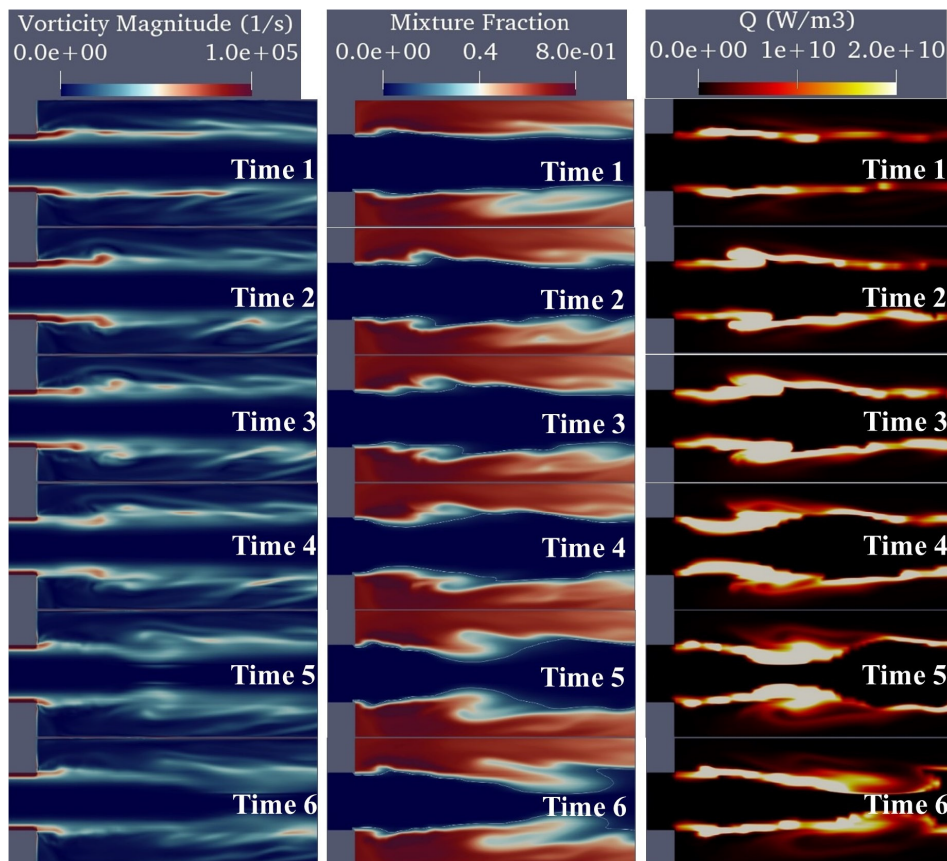
FIG. 19. Cycle snapshots for case 2 during the non-oscillation state in intermittency. Left image: vorticity magnitude (1/s). Middle image: mixture fraction. Right image: heat release rate (W/m^3).

and, therefore, large-scale coherent structures are observed, resulting in an abrupt heat release. At moments T2, T4, and T5, the high-pressure waves propagate downstream of the combustion chamber and, therefore, no wrinkled flame surface is observed near the dump plane. Subsequently, at the moment T6, the time-synchronous process of the combustion flow fields over one cycle within period-2 oscillations is completed.

V. CONCLUSIONS

In this paper, three-dimensional large eddy simulation algorithms combined with the Euler–Lagrange framework are carried out to treat turbulent spray combustion processes in a single-element liquid rocket engine, based on the open-source platform OpenFOAM-6 with a modified version of SprayFOAM. After verification of the numerical framework and grid independence, the equivalence ratio (ϕ) is used as a control parameter and is continuously varied to encompass from fuel-rich ($\phi = 1.5$) to fuel-lean ($\phi = 0.5$). We observe that the transition of dynamical states from period-1 oscillations ($\phi = 1.5$) to eventually period-2 states ($\phi = 0.5$) is via intermittency ($1.3 \leq \phi \leq 0.9$). In particular, transient modes switching between period-1 (P1) and period-2 (P2) was also observed when the equivalence ratio was 0.7 ($\phi = 0.7$). Based on the simultaneous examination of the pressure traces and the multiple subsystems of the combustion flow field, the following conclusions can be also obtained.

1. During the P1 thermoacoustic instability, the vortex shedding is dominated by the first-order longitudinal acoustic frequency (1L). The consequent high-amplitude acoustic oscillations cause a cyclical increase in temperature and mass fraction of the species at the shear layer. This, in turn, steepens the compression wave front, which is represented in the phase portraits diagram of the combustion subsystem, such as temperature and mass fraction of reactants.

2. During the intermittency, the system dynamics transition between P1 and aperiodic oscillations. The vortex shedding frequency remains at the 1L acoustic frequency during the periodic portion of intermittency. By contrast, the vortex dynamics are governed by combustion noise during the aperiodic portion of intermittency.

3. During the P2 thermoacoustic instability, the vortex shedding is dominated by the second-order longitudinal acoustic frequency (2L). At an equivalence ratio of 0.5, the vortex shedding frequency remains at the frequency of the 1L acoustic mode initially and later shifts from the 1L mode to the 2L mode, eventually leading to the P2 oscillation.

4. The intricate nonlinear dynamical states, including period-1, period-2, and intermittency, are found to be caused by the mutual synchronization between the acoustic field and the flame heat release rate. As the equivalence ratio gradually decreases, the bidirectional coupling between these subsystems leads to a
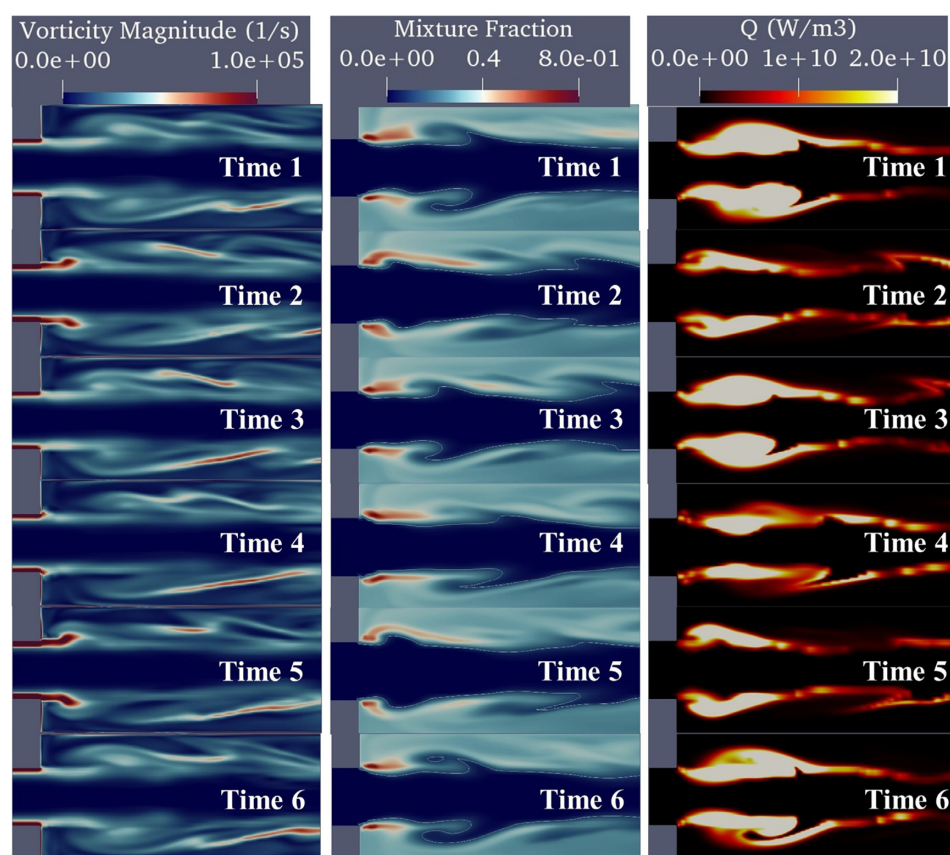
FIG. 20. Cycle snapshots during the period-2 oscillation in case 7. Left image: vorticity magnitude (1/s). Middle image: mixture fraction. Right image: heat release rate (W/m^3).

dynamic transition from intermittency to synchronization with period-2 oscillations. The analysis of cycle snapshots also offers additional information about the synchronization processes that take place between the pressure and several subsystems, such as vortex dynamics, mixture fraction, and combustion heat release. Moreover, the emergence of a large-scale coherent structure between several subsystems of the combustion flow field is also responsible for driving the period-n oscillations.

AUTHOR DECLARATIONS
Conflict of Interest

The authors have no conflicts to disclose.

Author Contributions

Yuanzhe Liu: Conceptualization (lead); Data curation (equal); Formal analysis (equal); Funding acquisition (equal); Investigation (equal); Methodology (equal); Project administration (equal); Software (equal); Supervision (equal); Validation (equal); Visualization (equal); Writing – original draft (equal); Writing – review & editing (equal). **Pei-jin Liu:** Funding acquisition (lead); Supervision (equal); Writing – review & editing (equal). **Zhuopu Wang:** Conceptualization (lead); Data curation (equal); Formal analysis (equal); Funding acquisition (equal); Investigation (equal); Methodology (equal); Project administration (equal); Software (equal); Supervision (equal); Validation (equal); Visualization (equal); Writing – original draft (equal); Writing – review & editing (equal). **Wen Ao:** Writing – review & editing (equal). **Yu Guan:** Supervision (equal); Writing – review & editing (equal).

DATA AVAILABILITY

The data that support the findings of this study are available from the corresponding author upon reasonable request.

REFERENCES

[1]K. Manoj, S. A. Pawar, J. Kurths, and R. I. Sujith, "Rijke tube: A nonlinear oscillator," Chaos **32**(7), 072101 (2022).

[2]C. Ruan, F. Chen, W. Cai, Y. Qian, L. Yu, and X. Lu, "Principles of non-intrusive diagnostic techniques and their applications for fundamental studies of combustion instabilities in gas turbine combustors: A brief review," Aerosp. Sci. Technol. **84**, 585–603 (2019).

[3]W. A. Sirignano, "Driving mechanisms for combustion instability," Combust. Sci. Technol. **187**(1–2), 162–205 (2015).

[4]J. O'Connor, V. Acharya, and T. Lieuwen, "Transverse combustion instabilities: Acoustic, fluid mechanic, and flame processes," Prog. Energy Combust. Sci. **49**, 1–39 (2015).

[5]M. Bauerheim, F. Nicoud, and T. Poinsot, "Progress in analytical methods to predict and control azimuthal combustion instability modes in annular chambers," Phys. Fluids **28**(2), 021303 (2016).

[6]T. Poinsot, "Prediction and control of combustion instabilities in real engines," Proc. Combust. Inst. **36**(1), 1–28 (2017).

[7]M. Klein, N. Chakraborty, A. Kempf, and A. Sadiki, "Development and validation of models for turbulent reacting flows," Phys. Fluids **34**(12), 120401 (2022).

[8]D. Zhao and Y. Guan, "Characterizing modal exponential growth behaviors of self-excited transverse and longitudinal thermoacoustic instabilities," Phys. Fluids **34**(2), 024109 (2022).

[9]K. Guo, L. Ni, Y. Ren, W. Lin, Y. Tong, and W. Nie, "Experimental investigation on effects of injection distribution on combustion instability in a model rocket combustor," Phys. Fluids **34**(1), 011702 (2022).

[10]F. E. C. Culick and V. Yang, *Overview of Combustion Instabilities in Liquid-Propellant Rocket Engines* (American Institute of Aeonautics & Astrophysics, 1995).

[11]X.-Y. Guan, B.-Q. Jia, L.-J. Yang, and Q.-F. Fu, "Linear instability of an annular liquid jet with gas velocity oscillations," Phys. Fluids **33**(5), 054110 (2021).

[12]A. Kureshee, S. Narayanan, and D. K. Mandal, "Evaporation of twin drops: Effect of acoustics and spacing," Phys. Fluids **35**(3), 032103 (2023).

[13]P. Kasthuri, A. Krishnan, R. Gejji, W. Anderson, N. Marwan, J. Kurths, and R. I. Sujith, "Investigation into the coherence of flame intensity oscillations in a model multi-element rocket combustor using complex networks," Phys. Fluids **34**, 034107 (2022).

[14]X. Wang, Y. Wang, and V. Yang, "Three-dimensional flow dynamics and mixing in a gas-centered liquid-swirl coaxial injector at supercritical pressure," Phys. Fluids **31**(6), 065109 (2019).

[15]C. O. Paschereit, E. Gutmark, and W. Weisenstein, "Coherent structures in swirling flows and their role in acoustic combustion control," Phys. Fluids **11**(9), 2667–2678 (1999).

[16]K. C. Schadow, E. Gutmark, T. P. Parr, D. M. Parr, K. J. Wilson, and J. E. Crump, "Large-scale coherent structures as drivers of combustion instability," Combust. Sci. Technol. **64**(4–6), 167–186 (1989).

[17]Lord Rayleigh and N. H. Nachtrieb, "The theory of sound," Phys. Today **10**(1), 32–34 (1957).

[18]T. Lieuwen, "Modeling premixed combustion-acoustic wave interactions: A review," J. Propul. Power **19**(5), 765–781 (2003).

[19]J. Li, Y. Xia, A. S. Morgans, and X. Han, "Numerical prediction of combustion instability limit cycle oscillations for a combustor with a long flame," Combust. Flame **185**, 28–43 (2017).

[20]X. Han, J. Li, and A. S. Morgans, "Prediction of combustion instability limit cycle oscillations by combining flame describing function simulations with a thermoacoustic network model," Combust. Flame **162**(10), 3632–3647 (2015).

[21]M. L. Frezzotti, F. Nasuti, C. Huang, C. L. Merkle, and W. E. Anderson, "Quasi-1D modeling of heat release for the study of longitudinal combustion instability," Aerosp. Sci. Technol. **75**, 261–270 (2018).

[22]S.-K. Kim, D. Kim, and D. J. Cha, "Finite element analysis of self-excited instabilities in a lean premixed gas turbine combustor," Int. J. Heat Mass Transfer **120**, 350–360 (2018).

[23]R. I. Sujith and V. R. Unni, "Complex system approach to investigate and mitigate thermoacoustic instability in turbulent combustors," Phys. Fluids **32**(6), 061401 (2020).

[24]M. P. Juniper and R. I. Sujith, "Sensitivity and nonlinearity of thermoacoustic oscillations," Annu. Rev. Fluid Mech. **50**, 661–689 (2018).

[25]V. Nair and R. I. Sujith, "Multifractality in combustion noise: Predicting an impending combustion instability," J. Fluid Mech. **747**, 635–655 (2014).

[26]L. Kabiraj and R. I. Sujith, "Nonlinear self-excited thermoacoustic oscillations: Intermittency and flame blowout," J. Fluid Mech. **713**, 376–397 (2012).

[27]S. A. Pawar, M. Raghunathan, K. V. Reeja, P. R. Midhun, and R. I. Sujith, "Effect of preheating of the reactants on the transition to thermoacoustic instability in a bluff-body stabilized dump combustor," Proc. Combust. Inst. **38**(4), 6193–6201 (2021).

[28]S. A. Pawar, A. Seshadri, V. R. Unni, and R. I. Sujith, "Thermoacoustic instability as mutual synchronization between the acoustic field of the confinement and turbulent reactive flow," J. Fluid Mech. **827**, 664–693 (2017).

[29]L. Kabiraj, A. Saurabh, P. Wahi, and R. I. Sujith, "Route to chaos for combustion instability in ducted laminar premixed flames," Chaos **22**(2), 023129 (2012).

[30]V. Nair, G. Thampi, and R. I. Sujith, "Intermittency route to thermoacoustic instability in turbulent combustors," J. Fluid Mech. **756**, 470–487 (2014).

[31]C. P. Premchand, N. B. George, M. Raghunathan, V. R. Unni, R. I. Sujith, and V. Nai, "Lagrangian analysis of intermittent sound sources in the flow-field of a bluff-body stabilized combustor," Phys. Fluids **31**, 025115 (2019).

[32]H. Gotoda, M. Amano, T. Miyano, T. Ikawa, K. Maki, and S. Tachibana, "Characterization of complexities in combustion instability in a lean premixed gas-turbine model combustor," Chaos **22**(4), 043128 (2012).

[33]H. Gotoda, Y. Shinoda, M. Kobayashi, Y. Okuno, and S. Tachibana, "Detection and control of combustion instability based on the concept of dynamical system theory," Phys. Rev. E: Stat., Nonlinear, Soft Matter Phys. **89**(2), 022910 (2014).

[34]H. Gotoda, H. Nikimoto, T. Miyano, and S. Tachibana, "Dynamic properties of combustion instability in a lean premixed gas-turbine combustor," Chaos **21**(1), 013124 (2011).

[35]Y. Nomi, H. Gotoda, S. Fukuda, and C. Almarcha, "Complex network analysis of spatiotemporal dynamics of premixed flame in a Hele–Shaw cell: A transition from chaos to stochastic state," Chaos **31**(12), 123133 (2021).

[36]L. Kabiraj, R. I. Sujith, and P. Wahi, "Bifurcations of self-excited ducted laminar premixed flames," J. Eng. Gas Turbines Power **134**, 031502 (2012).

[37]Y. Guan, V. Gupta, and L. K. B. Li, "Intermittency route to self-excited chaotic thermoacoustic oscillations," J. Fluid Mech. **894**, R3 (2020).

[38]Y. Guan, P. Liu, B. Jin, V. Gupta, and L. K. B. Li, "Nonlinear time-series analysis of thermoacoustic oscillations in a solid rocket motor," Exp. Therm. Fluid Sci. **98**, 217–226 (2018).

[39]P. Kasthuri, I. Pavithran, S. A. Pawar, R. I. Sujith, R. Gejji, and W. Anderson, "Dynamical systems approach to study thermoacoustic transitions in a liquid rocket combustor," Chaos **29**(10), 103115 (2019).

[40]S. Shima, K. Nakamura, H. Gotoda, Y. Ohmichi, and S. Matsuyama, "Formation mechanism of high-frequency combustion oscillations in a model rocket engine combustor," Phys. Fluids **33**(6), 064108 (2021).

[41]S. Menon, "Subgrid combustion modelling for large-eddy simulations," Int. J. Engine Res. **1**, 209 (2000).

[42]C. Gong, M. Jangi, and X.-S. Bai, "Large eddy simulation of n-Dodecane spray combustion in a high pressure combustion vessel," Appl. Energy **136**, 373–381 (2014).

[43]N. Kim, K. Jung, and Y. Kim, "Multi-environment PDF modeling for n-dodecane spray combustion processes using tabulated chemistry," Combust. Flame **192**, 205–220 (2018).

[44]F. L. Sacomano Filho, A. Hosseinzadeh, A. Sadiki, and J. Janicka, "On the interaction between turbulence and ethanol spray combustion using a dynamic wrinkling model coupled with tabulated chemistry," Combust. Flame **215**, 203–220 (2020).

[45]W. Zhao, H. Wei, M. Jia, Z. Lu, K. H. Luo, R. Chen, and L. Zhou, "Flame–spray interaction and combustion features in split-injection spray flames under diesel engine-like conditions," Combust. Flame **210**, 204–221 (2019).

[46]Y. Liu, P. Liu, Z. Wang, G. Xu, and B. Jin, "Numerical investigation of mode competition and cooperation on the combustion instability in a non-premixed combustor," Acta Astronaut. **198**, 271–285 (2022).

[47]C.-W. Tsang, M. F. Trujillo, and C. J. Rutland, "Large-eddy simulation of shear flows and high-speed vaporizing liquid fuel sprays," Comput. Fluids **105**, 262–279 (2014).

[48]G. Xu, P. Liu, W. Ao, Z. Wang, and B. Jin, "Numerical investigation of thermoacoustic instability caused by small disturbance in a solid rocket motor," Aerosp. Sci. Technol. **113**, 106678 (2021).

[49]G. Xu, P. Liu, W. Ao, and B. Jin, "Interactions between turbulent flow and diffusion flame of composite propellant in a solid rocket motor with sidewall mass injection," Aerosp. Sci. Technol. **102**, 105872 (2020).

[50]K. Miller, J. Sisco, N. Nugent, and W. Anderson, "Experimental study of combustion instabilities in a single-element coaxial swirl injector," AIAA Paper No. 2005-4298, 2005.

[51]K. Guo, B. Xu, Y. Ren, Y. Tong, and W. Nie, "Analysis of tangential combustion instability modes in a LOX/kerosene liquid rocket engine based on OpenFOAM," Front. Energy Res. **9**, 810439 (2022).

[52]R. Smith, G. Xia, W. A. Anderson, and C. L. Merkle, "Computational simulations of the effect of backstep height on nonpremixed combustion instability," AIAA J. **48**(9), 1857–1868 (2010).

[53]M. E. Harvazinski, C. Huang, V. Sankaran, T. W. Feldman, W. E. Anderson, C. L. Merkle, and D. G. Talley, "Coupling between hydrodynamics, acoustics, and

heat release in a self-excited unstable combustor," Phys. Fluids **27**(4), 045102 (2015).

[54]K. Guo, Y. Ren, Y. Tong, W. Lin, and W. Nie, "Analysis of self-excited transverse combustion instability in a rectangular model rocket combustor," Phys. Fluids **34**(4), 047104 (2022).

[55]T. Yao, Y. Pei, B.-J. Zhong, S. Som, T. Lu, and K. H. Luo, "A compact skeletal mechanism for n-dodecane with optimized semi-global low-temperature chemistry for diesel engine simulations," Fuel **191**, 339–349 (2017).

[56]Y. Yalcinkaya and A. G. Gungor, "Pressure gradient effect on flame–vortex interaction in lean premixed bluff-body stabilized flames," Phys. Fluids **35**, 045105 (2023).

[57]B. Wu, X. Zhao, B. R. Chowdhury, B. M. Cetegen, C. Xu, and T. Lu, "A numerical investigation of the flame structure and blowoff characteristics of a bluff-body stabilized turbulent premixed flame," Combust. Flame **202**, 376–393 (2019).

[58]R. Smith, M. Ellis, G. Xia, V. Sankaran, W. Anderson, and C. L. Merkle, "Computational investigation of acoustics and instabilities in a longitudinal-mode rocket combustor," AIAA J. **46**(11), 2659–2673 (2008).

13 January 2025 07:09:57